The potassic sedimentary rocks in Gale Crater, Mars, as seen by ChemCam on board Curiosity

L. Le Deit, N. Mangold, O. Forni, A. Cousin, J. Lasue, S. Schröder, R. Wiens, D. Sumner, C. Fabre, K. Stack, et al.

AGU PUBLICATIONS

JGR

Journal of Geophysical Research: Planets

RESEARCH ARTICLE
10.1002/2015JE004987

Special Section:
The Mars Science Laboratory Rover Mission (Curiosity) at The Kimberley, Gale Crater, Mars

The potassic sedimentary rocks in Gale Crater, Mars, as seen by ChemCam on board *Curiosity*

L. Le Deit[1], N. Mangold[1], O. Forni[2], A. Cousin[2], J. Lasue[2], S. Schröder[2,3], R. C. Wiens[4], D. Sumner[5], C. Fabre[6], K. M. Stack[7], R. B. Anderson[8], D. Blaney[7], S. Clegg[4], G. Dromart[9], M. Fisk[10], O. Gasnault[2], J. P. Grotzinger[11], S. Gupta[12], N. Lanza[4], S. Le Mouélic[1], S. Maurice[2], S. M. McLennan[13], P.-Y. Meslin[2], M. Nachon[1], H. Newsom[14], V. Payré[6], W. Rapin[2], M. Rice[15], V. Sautter[16], and A. H. Treiman[17]

[1]Laboratoire de Planétologie et Géodynamique, LPG-Nantes, UMR CNRS 6112, Université de Nantes, Nantes, France, [2]Institut de Recherche en Astrophysique et Planétologie, Toulouse, France, [3]German Aerospace Center (DLR), Institut für Optische Sensorsysteme, Berlin-Adlershof, Germany, [4]Los Alamos National Laboratory, Los Alamos, New Mexico, USA, [5]Earth and Planetary Sciences, University of California, Davis, California, USA, [6]GeoRessources, Université de Lorraine, Nancy, France, [7]Jet Propulsion Laboratory, California Institute of Technology, Pasadena, California, USA, [8]U.S. Geological Survey Astrogeology Science Center, Flagstaff, Arizona, USA, [9]Laboratoire de Géologie de Lyon, Terre, Planètes, Environnement, ENS Lyon, Lyon, France, [10]College of Earth, Ocean, and Atmospheric Sciences, Oregon State University, Corvallis, Oregon, USA, [11]Division of Geologic and Planetary Sciences, California Institute of Technology, Pasadena, California, USA, [12]Imperial College London, London, UK, [13]Department of Geosciences, State University of New York at Stony Brook, Stony Brook, New York, USA, [14]Institute of Meteoritics, University of New Mexico, Albuquerque, New Mexico, USA, [15]Geology Department, Western Washington University, Bellingham, Washington, USA, [16]LMCM, Muséum d'Histoire Naturelle, Paris, France, [17]Lunar and Planetary Institute, Houston, Texas, USA

Key Points:
- Mean K_2O abundance in sedimentary rocks >5 times higher than that of the average Martian crust
- Presence of alkali feldspars and K-phyllosilicates in basaltic sedimentary rocks along the traverse
- The K-bearing minerals likely have a detrital origin

Correspondence to:
L. Le Deit,
Laetitia.Ledeit@univ-nantes.fr

Citation:
Le Deit, L., et al. (2016), The potassic sedimentary rocks in Gale Crater, Mars, as seen by ChemCam on board *Curiosity*, *J. Geophys. Res. Planets*, *121*, 784–804, doi:10.1002/2015JE004987.

Received 11 DEC 2015
Accepted 30 MAR 2016
Published online 13 MAY 2016

Abstract The Mars Science Laboratory rover *Curiosity* encountered potassium-rich clastic sedimentary rocks at two sites in Gale Crater, the waypoints Cooperstown and Kimberley. These rocks include several distinct meters thick sedimentary outcrops ranging from fine sandstone to conglomerate, interpreted to record an ancient fluvial or fluvio-deltaic depositional system. From ChemCam Laser-Induced Breakdown Spectroscopy (LIBS) chemical analyses, this suite of sedimentary rocks has an overall mean K_2O abundance that is more than 5 times higher than that of the average Martian crust. The combined analysis of ChemCam data with stratigraphic and geographic locations reveals that the mean K_2O abundance increases upward through the stratigraphic section. Chemical analyses across each unit can be represented as mixtures of several distinct chemical components, i.e., mineral phases, including K-bearing minerals, mafic silicates, Fe-oxides, and Fe-hydroxide/oxyhydroxides. Possible K-bearing minerals include alkali feldspar (including anorthoclase and sanidine) and K-bearing phyllosilicate such as illite. Mixtures of different source rocks, including a potassium-rich rock located on the rim and walls of Gale Crater, are the likely origin of observed chemical variations within each unit. Physical sorting may have also played a role in the enrichment in K in the Kimberley formation. The occurrence of these potassic sedimentary rocks provides additional evidence for the chemical diversity of the crust exposed at Gale Crater.

1. Introduction

The Mars Science Laboratory (MSL) rover, *Curiosity*, has been investigating the northwestern plain of Gale Crater, Aeolis Palus, since August 2012 (Figure 1a). The landing site, named Bradbury landing, is located at the distal portions of a set of alluvial fans located at the outlet of Peace Vallis, a fluvial channel cutting through the northwestern rim and wall of Gale Crater [*Palucis et al.*, 2014; *Grotzinger et al.*, 2015]. Shortly after landing, Curiosity encountered fine-grained clastic sedimentary rocks of the Yellowknife Bay (YKB) formation. Ranging from mudstones at the base to sandstones at the top, this formation includes an ancient fluvio-lacustrine system that would have been habitable [*Grotzinger et al.*, 2014, 2015]. YKB rocks were derived from basaltic sources and postdepositional aqueous alteration took place at low water/rock ratios under nearly isochemical conditions, suggesting arid, possibly cold, paleoclimates, and rapid erosion/deposition [*McLennan et al.*, 2013].

The first sedimentary rocks enriched in K relative to the average Martian crust were encountered in the uppermost member of the YKB formation at three outcrops, namely, Shaler, Rocknest, and Bathurst Inlet. Ranging from massive siltstone to coarse and cross-bedded sandstone, they have heterogeneous facies

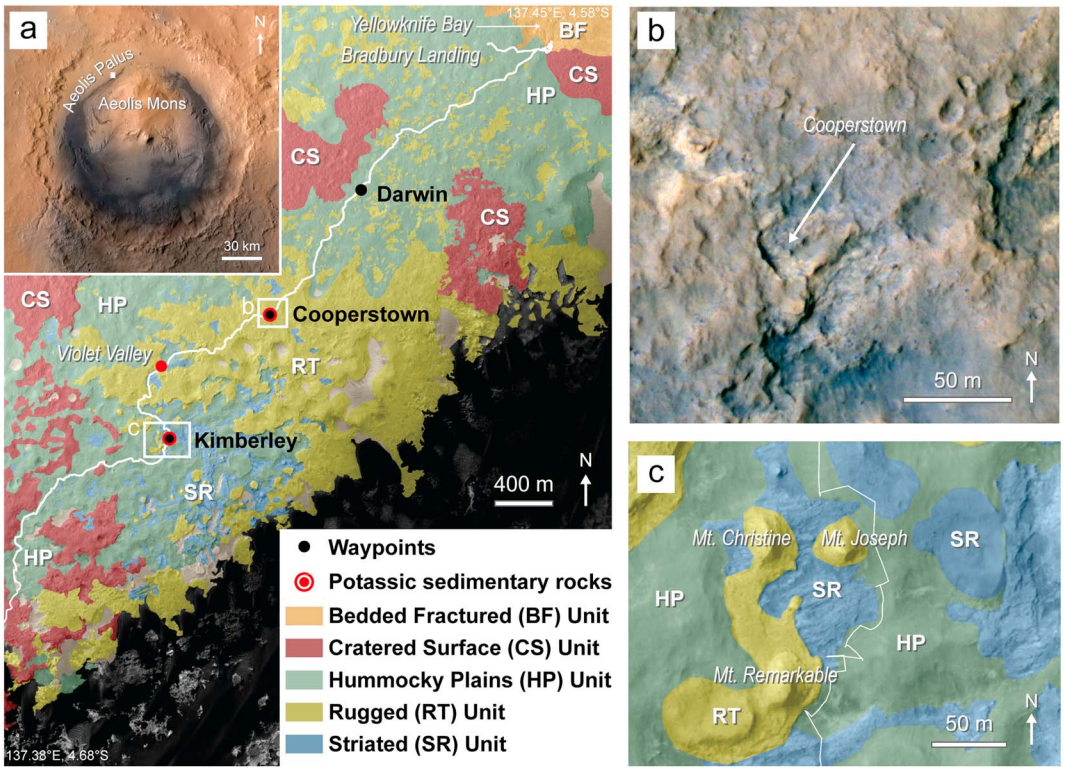

Figure 1. Location and geologic context of potassic sedimentary rocks. (a) Location of potassic sedimentary rocks identified using ChemCam data along *Curiosity* traverse (white line) plotted over a geological map of the landing area [*Grotzinger et al.*, 2014]. Each unit is detailed in *Grotzinger et al.* [2014]. Location of Figures 1b and 1c is indicated. Location of the landing area is shown (inset) on a mosaic of Gale Crater (NASA/JPL-Caltech/ESA/DLR/FU Berlin/MSSS). (b) HiRISE IRB (ESP_028678_1755) image of Cooperstown. (c) Close-up view of Figure 1a showing the Kimberley waypoint.

and chemistry [*Blaney et al.*, 2014; *Schmidt et al.*, 2014; *Anderson et al.*, 2015a; *Mangold et al.*, 2015; *Sautter et al.*, 2013]. Their K_2O abundances range between 0.7 and 1.1 wt % [*Mangold et al.*, 2015], which is significantly greater than that of the average Martian crust that is around 0.45 wt % [*Taylor and McLennan*, 2009], and suggest the presence of a K-feldspar, mica, or K-rich glass fragments in these rocks. The composition in major elements of the average Martian crust was estimated from the average composition of soils analyzed by the Mars Exploration Rovers and gamma ray spectra mapping from Mars Odyssey [*Hahn and McLennan*, 2007; *Taylor and McLennan*, 2009].

From the landing site, Curiosity achieved a ~9 km traverse along Aeolis Palus before reaching the contact with the Murray formation which defines the oldest strata at the base of Aeolis Mons (also informally named Mount Sharp), a crescent-shaped mound of layered deposits up to 5 km high [*Grotzinger et al.*, 2015, Figure 1a]. Curiosity explored the hummocky plains (HP) unit that is tonally smooth and has lower values of thermal inertia than the YKB formation [*Grotzinger et al.*, 2014]. Outcrops encountered in the HP unit correspond to fluvial conglomerates bearing pebbles of various compositions but dominated by plagioclase mineralogy [*Williams et al.*, 2013; *Mangold et al.*, 2016]. The higher abundance of Mg in clastic fracture fills cutting conglomerates suggests late episodes of postdepositional aqueous alteration possibly coeval with that of YKB [*Mangold et al.*, 2016]. Curiosity also analyzed float igneous rocks containing a significant feldspar component and corresponding to two distinct geochemical series [*Sautter et al.*, 2015]. The first is rich in plagioclase and contains excess silica, putting it close to granodiorite in composition; the second series is an alkaline K-feldspar-bearing suite [*Sautter et al.*, 2015].

On its way to Aeolis Mons Curiosity reached other exposures of rocks significantly enriched in K [e.g., *Le Deit et al.*, 2015]. Our objective in this study is to explore the spatial distributions of those rocks, their chemical composition, and their relationships with previously investigated rocks in terms of composition, stratigraphy,

source rocks, and alteration history. The Chemistry and Camera (ChemCam) instrument on board Curiosity allows for the remote analysis of the elemental composition of rocks and soils [*Wiens et al*., 2012; *Maurice et al*., 2012]. More than 700 ChemCam observation points have been acquired on these potassic rocks, which provide a significant sampling for constraining their spatial and chemical variability. First, we present the ChemCam data and methods used for classifying these data and for deriving quantitative estimations of the chemical compositions (section 2). Then, we report the geologic context, stratigraphy, and facies of the potassic sedimentary rocks (section 3), followed by a synthesis of the chemical composition of these rocks, as seen by ChemCam according to their stratigraphic position (section 4). Finally, we discuss the possible origins of this enrichment in K in terms of source rocks and alteration processes (section 5).

2. ChemCam Data and Methods

2.1. Instrument Description and Data Acquisition

The ChemCam instrument suite on Curiosity combines a remote Laser-induced breakdown spectrometer (LIBS) capable of determining elemental compositions of rocks and soils within 7 m of the instrument, as well as a Remote Micro-Imager (RMI) for high-resolution imaging [*Wiens et al*., 2012; *Maurice et al*., 2012]. The LIBS uses the radiation of a Q-switched Nd:KGW pulsed laser at the top of the mast focused on a target to ablate material and produce atoms and ions in an excited state. The decay of these atoms back to ground state produces emission light which is collected and transmitted to three dispersive spectrometers covering the ultraviolet (UV; 240–342 nm), violet and blue (VIO; 382–469 nm), and visible/near-infrared (VNIR; 474–906 nm) spectral regions [*Wiens et al*., 2012], allowing the identification of the characteristic emission lines of the elements present in the sample. The ChemCam LIBS spectra are automatically preprocessed by subtracting the ambient light background, removing noise using a wavelet transform method, removing the electron continuum, calibrating for the wavelength, correcting for the variable distance to the target, and applying a wavelength-dependent correction for the instrument response [*Wiens et al*., 2013]. Laser ablation creates pits on the target's surface between 300 and 600 μm in diameter at those distances and these vary in depth according to the rheology of the target material. Each ChemCam LIBS point (or pit) corresponds typically to a burst of 30 shots used to collect 30 spectra at the same location. The first five spectra show contamination by dust [*Meslin et al*., 2013; *Lasue et al*., 2014] and are thus not taken into account in the average spectrum of each point. ChemCam observations correspond typically to line scans of 5 or 10 points, or matrices of 3×3, 4×4, or 5×5 points, providing data on the chemical variability within each target as well as its bulk composition.

The ChemCam instrument also includes a RMI that provides context panchromatic images to the LIBS points, allowing to analyze the texture of the target's surface [*Wiens et al*., 2012; *Maurice et al*., 2012]. Features as small as 120 μm (identified by 2 pixels) can be resolved for targets located at ~3 m from the instrument [*Le Mouélic et al*., 2015].

2.2. Data Processing

2.2.1. Major Element Compositions

The ChemCam team recently completed a revised calibration model for the major elements [*Wiens et al*., 2013; *Anderson et al*., 2014, 2015b]. The mean oxide compositions (MOCs data) are determined for SiO_2, TiO_2, Al_2O_3, FeO_T, MgO, CaO, Na_2O, and K_2O using a combination of "submodel" partial least squares (SM-PLS) and independent component regression (ICR). SM-PLS uses submodels for each major element that are optimized for a limited range of sample compositions, rather than using a single "full" PLS model to predict all compositions from 0 to 100 wt %. By reducing the composition range of the PLS submodels, they can "specialize" in the spectral trends that are most relevant for that range, resulting in improved accuracy compared to a full model [*Anderson et al*., 2014, 2015b]. Independent component analysis (ICA) is a method of linear transformation in which the representation minimizes the statistical dependence of the components. The loadings are characterized by many LIBS emission lines of a single element. A relationship between the elemental ICA scores of a given spectrum and its composition can be derived [*Forni et al*., 2013]. Such relationships or regression laws have been derived for each element. The stability of the loadings has been verified to be very robust to any subsampling of the input database. The regression laws have been determined using an iterative scheme allowing an efficient removal of the potential outliers. The final best fit regression for each element was selected to satisfy the assumed Martian geological trends. To retrieve the

composition of a given ChemCam spectrum, the independent component regression (ICR) code computes for each element its score from the respective loading. The regression law is then applied to the score to obtain the composition [*Forni et al*., 2013]. The PLS1 and ICA calibration models represent two techniques that have both been in use since nearly the beginning of the mission. Because both techniques were well grounded in the training set while at the same time representing significantly different approaches, the combination of both techniques for the final product strengthens the overall result.

The PLS model uses as inputs a training set of standards observed using a laboratory version of the ChemCam instrument in Los Alamos. The ICR model uses a mixture of the new training set for some elements and the original database [*Wiens et al*., 2013] for other elements. The training set consists of up to 357 samples spanning a large range of compositions and comprised of both igneous and sedimentary sources.

To estimate the accuracy of the final, combined results, we selected a test set of training samples for each element that mimics the distribution of compositions in the full database. The PLS model was regenerated with these samples left out but with all parameters (number of components and normalization) remaining fixed. The ICA and PLS predictions for the test set samples are combined in the same manner as the predictions for unknown samples.

These combined predictions for the test set could be used to calculate a single root-mean-square error (RMSE) for each element. However, the performance of the calibration varies as a function of target composition, so a more representative estimate of the accuracy would be a RMSE that varies with predicted composition. The RMSE as a function of composition is calculated by using a moving window on the test set predictions.

The RMSE is given in the results of this paper. However, in many cases, such as when comparing the compositions of two different samples or units, the appropriate figure of merit is precision. For that reason we also provide precision with the results. Note that the Alpha Particle X-ray Spectrometer (APXS) typically only reports its precision and not its accuracy (corresponding to RMSE). Additionally, in cases where a number of points are averaged together, the standard deviation does not represent the precision of the technique, as it instead represents the heterogeneity of the samples. The standard deviations are also included with the averaged results.

The quantification of Mn was performed from an univariate calibration model, based on a dedicated calibration set of 26 standards with varying Mn contents analyzed with the ground laboratory version of the ChemCam instrument in Los Alamos after the methods of *Lanza et al*. [2014, 2015]. The limit of detection is approximately 0.06 wt % MnO, with an overall model RMSE of 9 wt % MnO and a RMSE of 1.1 wt % MnO for samples below 3 wt %.

2.2.2. Minor and Trace Element Compositions

The hydrogen signal-to-background ratio (SBR) was used in this work to estimate the hydrogen content of a given target [*Schröder et al*., 2015]. The SBR is a relative value obtained by dividing the hydrogen emission amplitude at 656.6 nm by the offset of the spectrum due to continuum radiation in manually processed ChemCam LIBS spectra. These H SBR values were compared within groups of targets sharing common features and similar matrices that were defined by cluster analysis of the ChemCam data of this work in the same way than described in detail in *Schröder et al*. [2015].

The abundance in Sr was estimated using the univariate model performed with the ChemCam Calibration Targets that are on board the rover [*Fabre et al*., 2014]. The RMSE for Sr is 659 ppm [*Ollila et al*., 2014].

The abundance of the other minor and trace elements documented in this study, i.e., Zn, F, Li, and Rb, was estimated using univariate quantification models generated from the analysis of dedicated sets of samples for each element with the ground laboratory version of ChemCam [*Wiens et al*., 2013; *Ollila et al*., 2014]. Each univariate model was based on a strong emission line characteristic of each element, including the emission line at 481.2 nm for Zn [*Lasue et al*., 2016], 603.1 nm for F [*Forni et al*., 2015a], 670.9 nm for Li [*Forni et al*., 2015b], and 780.2 nm for Rb. With this method, ChemCam's limit of detection is around 0.6 wt % for Zn, with a RMSE of 0.8 wt % for Zn, and 0.2 wt % for F. The detection limit of Li ranges between 0.3 and 25 ppm, with a RMSE of 36 ppm. Rb detection limit is around 20 ppm, with a RMSE of 52 ppm.

2.3. Approach

Apart from the three outcrops Shaler, Rocknest, and Bathurst Inlet analyzed in the early phase of the mission, potassic rocks were encountered along the traverse at three locations informally named Cooperstown

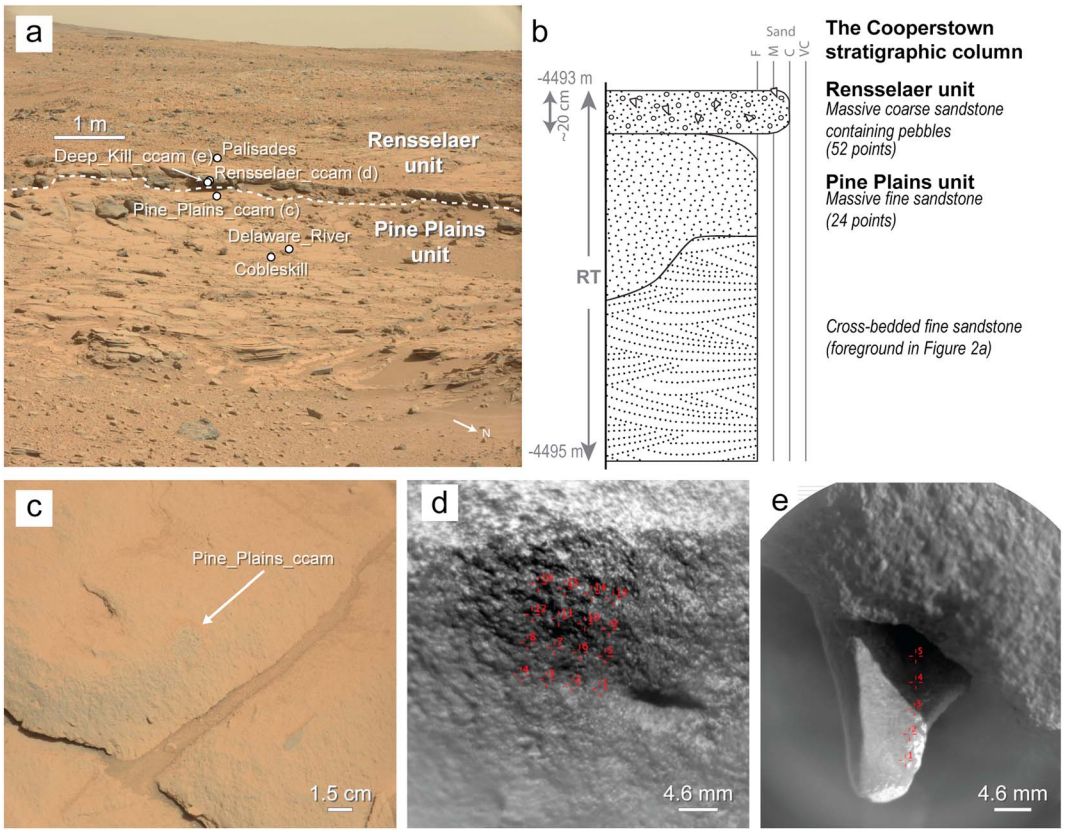

Figure 2. The Cooperstown outcrop. (a) Location of ChemCam targets indicated on a Mastcam image (0438ML1786002000E1_DXXX). White dashed line shows the contact between the lower Pine Plains unit and the upper Rensselaer unit corresponding to an overhang forming sandstone bed. (b) Interpretative stratigraphic column of the Cooperstown outcrop. The number of ChemCam LIBS points averaged for each unit is indicated (brackets). Approximate elevation of the full sedimentary column has been estimated by K. *Stack et al.* [2016]. Thickness of each member is not to scale. (c) Mastcam image (mcam01814.0000a.pine_plains_ccam_R0) of the ChemCam target Pine_Plains_ccam. (d) ChemCam RMI mosaic of the Rensselaer_ccam target (RMI images: CR0_436640651PRC_F0220000CCAM02441L1, CR0_436641357PRC_F0220000CCAM02441L1, CR0_436641760PRC_F0220000CCAM02441L1, CR0_436642522PRC_F0220000CCAM02441L1). (e) ChemCam RMI mosaic of the Deep_Kill_ccam target in the Rensselaer unit (RMI images: CR0_436828580PRC_F0220000CCAM03441L1, CR0_436828990PRC_F0220000CCAM03441L1, and CR0_436829447PRC_F0220000CCAM03441L1). ChemCam LIBS points are indicated (red).

(sols 438–453), Violet Valley (sol 550), and Kimberley (sols 576–632). A total of 744 ChemCam LIBS points was acquired on various target types including bedrocks, float rocks, fracture fills, soils, and drill tailings at these locations. In order to constrain the chemical variability according to stratigraphic and geographic location, only the points acquired on bedrock targets, i.e., 456 points, or 61% of the total number of points are taken into account for this study. All these ChemCam points distributed over 49 bedrock targets are classified according to their associated outcrop/geological formation and stratigraphic unit/member. Only 384 points of these 456 bedrock points were considered for the calculation of the H SBR values since they shared similar and hence, comparable matrices, as discussed in section 2.2.2 above. The stratigraphic units/members have been defined using the analysis of Mastcam, MAHLI, and ChemCam RMI images according to texture (i.e., grain size, sorting, and fabric), structure, bedding, and resistance to erosion of the exposed bedrocks. The occurrence of major stratigraphic contacts between the units/members is also observed in HiRISE orbital images [*Grotzinger et al.*, 2014].

3. Geologic Context, Stratigraphy, and Rock Facies

3.1. Cooperstown Outcrop

Cooperstown (−4.62°N, 137.42°E) is a waypoint along Curiosity's traverse occurring at the contact between light-toned outcrops and resistant darker outcrops visible in orbital HiRISE images (Figures 1a and 1b). The

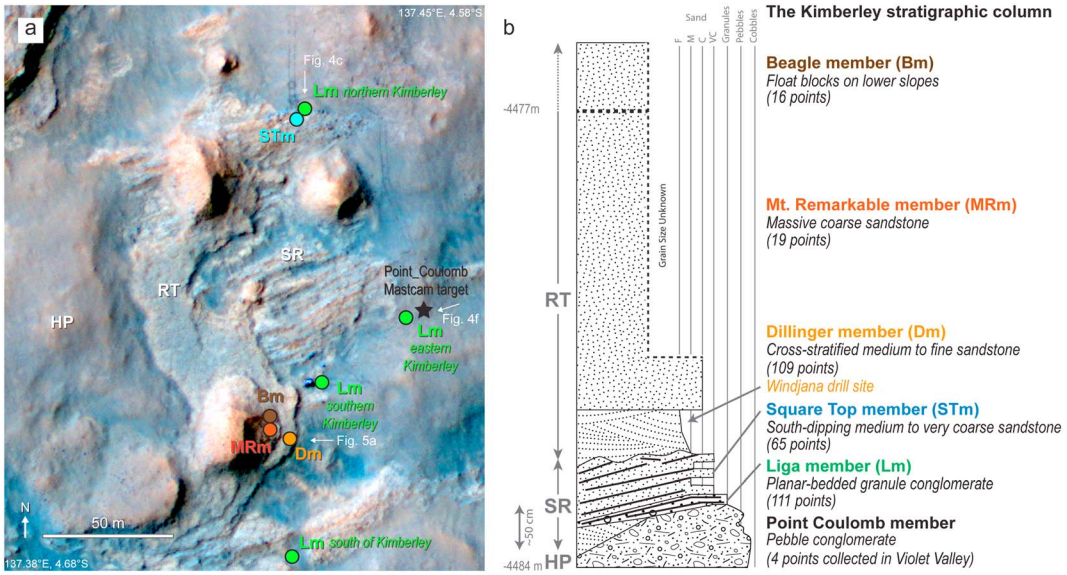

Figure 3. Stratigraphy of the Kimberley formation. (a) Location of the different targets investigated by ChemCam for each member (colored dots) shown on a HiRISE IRB image (ESP_036128_1755). Full unit names are detailed in Figure 1. *Curiosity* and its tracks are visible. (b) Interpretative stratigraphic column. Number of ChemCam LIBS points averaged for each member is indicated (brackets). Approximate elevation of the sedimentary column has been estimated by K. *Stack et al.* [2016].

Cooperstown outcrop is located within the "Rugged" map unit defined as light-toned topographically variable exposures [*Grotzinger et al.*, 2014].

The Cooperstown outcrop, defined on the ground, is divided into three units. The basal unit of the stratigraphic column is characterized by cross-bedded fine sandstone (Figures 2a and 2b). No ChemCam observation was acquired on this unit. It is overlain by the nearly flat-laying "Pine Plains unit," a massive fine sandstone with a homogeneous texture (Figures 2a–2c). At the top of the stratigraphic column, the "Rensselaer unit" is a 20 cm thick resistant ledge [*Stack et al.*, 2016] of well-cemented coarse sandstone containing pebbles and elongated voids (Figures 2a, 2b, 2d, and 2e). Pebbles are angular to platy, and the coarse sand is fairly well sorted and consists mostly of well-rounded grains. A relatively thin layer of sandstone, less resistant to erosion, lies between the Rensselaer and Pine Plains units (not represented in Figure 2b). It contains possible fracture fills and ventifacts. No ChemCam observations were acquired on this layer.

3.2. Kimberley Formation

Kimberley (−4.64°N, 137.4°E) is a waypoint located at ~1 km to the southwest of Cooperstown and is ~10 m higher in elevation than Cooperstown (Figures 1a, 1c, and 3). The Kimberley formation is also possibly stratigraphically above the Cooperstown outcrop [*Grotzinger et al.*, 2015; *Stack et al.*, 2016]. Kimberley stands out by the exposure of three major geomorphologic units visible from orbit: light-toned striated rocks or "Striated unit", an overlying Rugged unit, and the uppermost tonally smooth but hummocky unit, which is the Hummocky Plains (HP) unit [*Grotzinger et al.*, 2014, Figures 1c and 3a]. There are three mounds associated with the Rugged unit at Kimberley: Mount Christine and Mount Joseph to the north and the 3 m high Mount Remarkable to the south (Figures 1c and 3a).

The Kimberley formation includes six members, which in ascending stratigraphic order are the "Point Coulomb member"; the "Liga member" and the "Square Top member" (both associated with the Striated unit); the "Dillinger member" and the "Mount Remarkable member" (associated with the Rugged unit); and the "Beagle member" (Figure 3).

The lowermost member, the Point Coulomb, is a conglomerate with poorly rounded pebbles (Figures 3, 4a, and 4b). It has been observed with Mastcam at Kimberley and with ChemCam in the Violet Valley at an outcrop named "Bungle Bungle" (Figures 4a and 4b). It is poorly stratified and likely had significant topography on top of it prior to the deposition of the overlying Liga member.

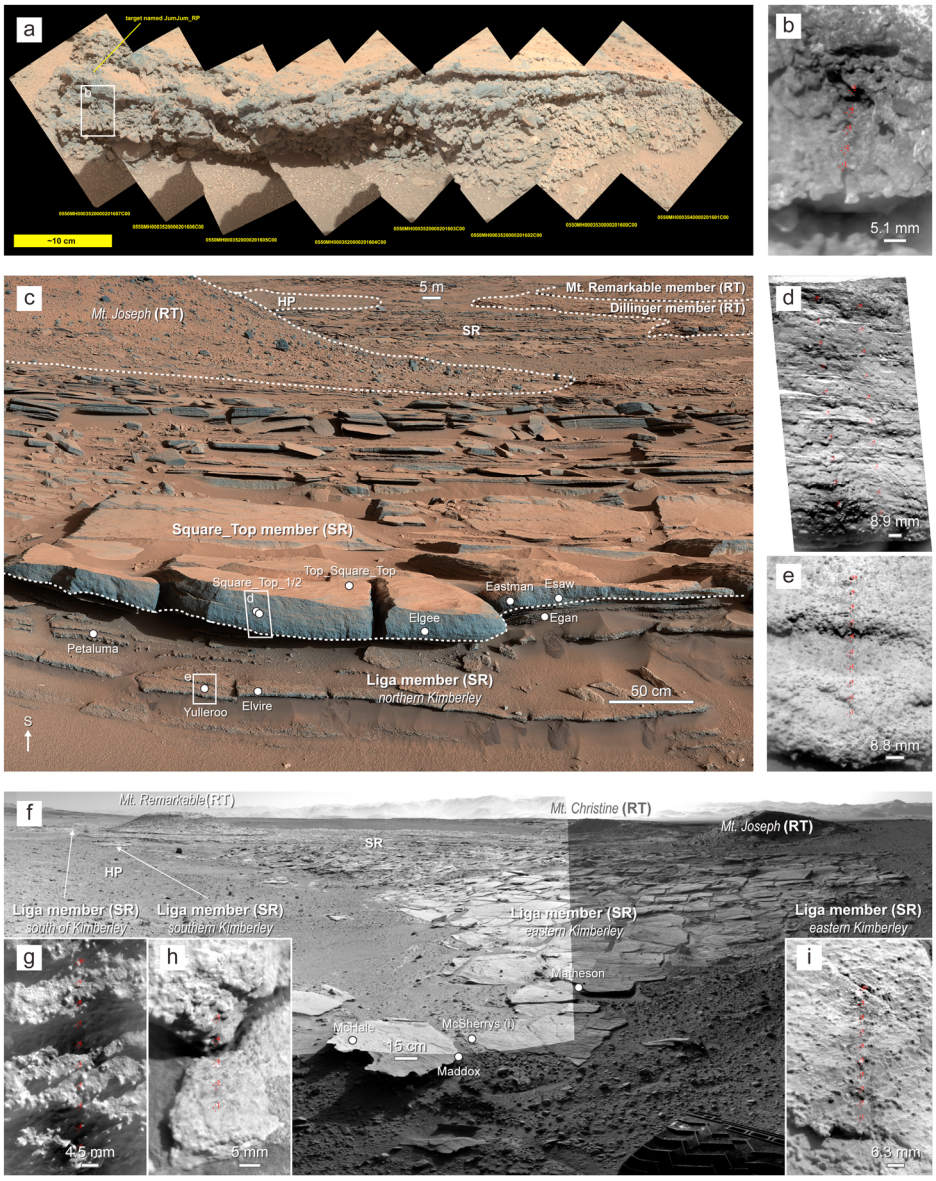

Figure 4. Facies of the lowermost members of the Kimberley formation: the Point_Coulomb, Liga, and Square Top members. (a) Mosaic of MAHLI images of the "Bungle Bungle" outcrop, in Violet Valley of the Point_Coulomb member; this is the site of the Jum_Jum target. (b) ChemCam RMI image of Jum_Jum (RMI images: CR0_446313251PRC_F0271004CCAM01550L2, CR0_446313840PRC_F0271004CCAM01550L2). (c) Mastcam panorama (mcam02407.0000b.kimberley_16x1_L0_41 × 6_L0_R0) of northern Kimberley showing the Liga and Square_Top members in the foreground and the Dillinger and Mount Remarkable members in the background. ChemCam bedrock targets of northern Kimberley are indicated by white dots. (d) ChemCam RMI images of the targets Square_Top and Square_Top_2 (RMI images: CR0_448625272PRC_F0300740CCAM01576L1, CR0_448625586PRC_F0300740CCAM01576L1, CR0_448625872PRC_F0300740CCAM01576L1, CR0_448626158PRC_F0300740CCAM01576L1, CR0_448626444PRC_F0300740CCAM01576L1, CR0_448626723PRC_F0300740CCAM01576L1, CR0_448894050PRC_F0300740CCAM04578L1, CR0_448894336PRC_F0300740CCAM04578L1, CR0_448894623PRC_F0300740CCAM04578L1, CR0_448894910PRC_F0300740CCAM04578L1, CR0_448895202PRC_F0300740CCAM04578L1, and CR0_448895482PRC_F0300740CCAM04578L1). (e) ChemCam RMI images of Yulleroo target (RMI images: CR0_448892557PRC_F0300740CCAM03578L1 and CR0_448893154PRC_F0300740CCAM03578L2). (f) View to the WSW of Kimberley showing the Liga member (outcrops of eastern, southern, and south of Kimberley, Navcam panorama). ChemCam bedrock targets of eastern Kimberley are indicated by white dots. (g) ChemCam RMI images of the Moogana target (RMI images: CR0_453603301PRC_F0320000CCAM01632L2, CR0_453603673PRC_F0320000CCAM01632L2, CR0_453604023PRC_F0320000CCAM01632L2, and CR0_453604432PRC_F0320000CCAM01632L1) (h) ChemCam RMI images of the Harms target (RMI images: CR0_450840163PRC_F0310724CCAM02601L1 and CR0_450840630PRC_F0310724CCAM02601L1). (i) ChemCam RMI images of the McSherrys target (RMI images: CR0_450222702PRC_F0310216CCAM02594L1, CR0_450223041PRC_F0310216CCAM02594L1, CR0_450223381PRC_F0310216CCAM02594L1, and CR0_450223381PRC_F0310216CCAM02594L1). ChemCam LIBS points are indicated (red) in Figure 4b, d, e, and g-i.

Journal of Geophysical Research: Planets

10.1002/2015JE004987

Table 1. List of ChemCam Targets on Bedrocks at Cooperstown and Kimberley[a]

Sol	Target	Outcrop/ Formation	Unit/Member	Sequence	Distance (m)	Obs. Type	# of Points	SiO_2	TiO_2	Al_2O_3	FeO_T	MgO	CaO	Na_2O	K_2O	Total
440	Delaware_River	Cooperstown	Pine Plains	ccam01440	3.55	4 × 4	16	43.3	1.3	8.5	23.8	8.4	4.9	2.2	0.9	93.3
440	Cobleskill	Cooperstown	Pine Plains	ccam02440	4.49	20 × 1	20	47.2	1.4	14.4	20.3	5.2	6.1	2.7	2.1	99.4
441	Pine_Plains_ccam	Cooperstown	Pine Plains	ccam01441	2.26	4 × 4	12	41.1	1.1	7.4	20.8	10.9	3.6	2.0	0.8	87.7
441	Rensselaer_ccam	Cooperstown	Rensselaer	ccam02441	2.32	4 × 4	13	42.1	1.0	7.7	21.1	9.0	4.8	1.9	1.0	88.5
441	Deep_Kill_ccam	Cooperstown	Rensselaer	ccam03441	2.33	1 × 5	5	41.6	1.2	8.5	21.9	6.7	4.0	2.0	1.3	87.2
453	Palisades	Cooperstown	Rensselaer	ccam01453	4.24	3 × 1	3	43.4	1.3	12.8	23.3	6.2	5.5	2.5	1.6	96.5
550	JumJum_ccam	Kimberley	Point Coulomb	ccam01550	2.60	5 × 1	5	47.2	0.8	15.9	21.3	2.4	2.5	4.3	1.9	96.5
578	Yulleroo	Kimberley	Liga—northern Kimberley	ccam03578	4.48	10 × 1	10	43.0	0.8	10.0	29.4	5.7	5.2	2.8	2.0	98.9
578	Petaluma	Kimberley	Liga—northern Kimberley	ccam05578	4.81	10 × 1	10	44.2	0.8	11.1	24.4	5.5	6.2	2.8	2.2	97.3
581	Egan	Kimberley	Liga—northern Kimberley	ccam01581	5.02	1 × 10	10	43.1	0.9	12.0	29.6	4.3	5.2	2.8	3.0	100.9
581	Elvire	Kimberley	Liga—northern Kimberley	ccam04581	4.45	1 × 5	5	44.5	0.9	9.7	25.4	6.0	5.9	2.1	2.1	96.8
583	Hooper	Kimberley	Liga—northern Kimberley	ccam01583	2.42	3 × 3	9	41.4	0.9	7.9	22.5	7.6	4.4	1.9	1.6	88.3
594	McHale	Kimberley	Liga—eastern Kimberley	ccam01594	3.18	3 × 3	9	45.9	0.7	9.7	20.2	9.4	5.1	2.2	1.7	94.9
594	McSherrys	Kimberley	Liga—eastern Kimberley	ccam02594	3.22	10 × 1	9	44.8	0.8	9.4	20.6	8.3	5.8	2.2	1.3	93.2
594	Matheson	Kimberley	Liga—eastern Kimberley	ccam03594	4.31	10 × 1	9	46.0	0.8	12.2	22.8	6.6	5.6	2.8	2.0	98.8
594	Maddox	Kimberley	Liga—eastern Kimberley	ccam05594	2.97	4 × 4	12	47.5	0.8	11.6	16.8	5.0	6.7	2.4	2.7	93.5
601	Liga	Kimberley	Liga—southern Kimberley	ccam01601	2.27	3 × 3	7	45.4	0.9	8.0	14.1	10.8	6.5	2.3	1.6	89.6
601	Harms	Kimberley	Liga—southern Kimberley	ccam02601	2.54	5 × 1	5	47.9	0.7	8.1	17.2	11.4	4.9	2.3	1.6	94.0
601	Nullara	Kimberley	Liga—southern Kimberley	ccam03601	2.95	3 × 3	9	47.7	0.7	7.6	15.2	11.7	6.5	2.7	1.7	93.7
601	Glidden	Kimberley	Liga—southern Kimberley	ccam04601	2.90	10 × 1	3	52.4	0.9	12.2	11.9	8.1	5.0	2.3	3.6	96.4
632	Moogana	Kimberley	Liga—south of Kimberley	ccam01632	2.29	10 × 1	8	45.7	0.8	8.0	16.9	8.1	6.8	1.9	2.7	90.8
632	Kalumburo	Kimberley	Liga—south of Kimberley	ccam02632	3.21	10 × 1	10	49.5	0.7	12.0	16.9	6.1	5.6	2.5	3.8	97.1
576	Square Top	Kimberley	Square Top	ccam01576	4.51	10 × 1	10	42.4	1.0	9.6	29.4	6.5	5.6	2.2	2.5	99.3
578	Square_Top_2	Kimberley	Square Top	ccam04578	4.47	10 × 1	10	44.2	0.9	10.0	26.0	6.7	6.0	2.2	2.9	98.9
581	Elgee	Kimberley	Square Top	ccam02581	4.58	10 × 1	10	43.2	0.9	9.8	27.9	7.4	5.4	2.2	2.6	99.5
585	Top_Square_Top	Kimberley	Square Top	ccam01585	2.43	3 × 3	9	42.0	0.9	7.4	20.9	7.2	6.1	1.6	1.5	87.7
585	Eastman	Kimberley	Square Top	ccam02585	2.50	20 × 1	20	40.6	0.9	6.9	22.3	8.3	5.5	1.6	1.9	88.0
585	Esaw	Kimberley	Square Top	ccam03585	2.58	3 × 3	9	40.6	0.9	7.5	22.3	7.9	5.4	1.7	1.8	88.1
608	Corrara	Kimberley	Dillinger	ccam01608	3.88	5 × 1	5	45.2	0.8	9.5	20.9	8.5	5.5	1.9	3.0	95.4
608	Forster	Kimberley	Dillinger	ccam02608	3.75	10 × 1	10	44.4	0.8	8.7	18.8	8.6	7.0	1.6	3.7	93.6
608	Fargoo	Kimberley	Dillinger	ccam03608	3.63	10 × 1	10	44.8	0.9	8.8	19.1	9.1	5.7	1.6	3.9	93.9
608	Wallal	Kimberley	Dillinger	ccam04608	3.16	5 × 1	5	46.8	0.9	9.0	19.4	8.8	4.4	2.0	3.6	94.9
608	Paperbark	Kimberley	Dillinger	ccam05608	3.45	10 × 1	10	43.4	0.8	8.0	17.6	9.4	8.0	1.1	3.3	91.6
608	Pentecost	Kimberley	Dillinger	ccam06608	3.58	10 × 1	10	46.7	0.9	9.2	19.1	8.9	4.9	1.5	3.8	95.1
609	Jarrad	Kimberley	Dillinger	ccam01609	3.70	10 × 1	10	44.2	0.9	8.9	20.7	9.6	4.6	1.5	3.8	94.3
609	Cow_Bore	Kimberley	Dillinger	ccam02609	3.53	10 × 1	10	44.1	0.9	9.0	19.4	8.3	6.4	1.3	3.3	92.6
611	Kevins_Dam	Kimberley	Dillinger	ccam02611	2.27	3 × 3	8	44.0	0.8	7.8	19.3	7.8	5.1	1.3	3.0	89.2
611	Thangoo	Kimberley	Dillinger	ccam03611	2.41	5 × 1	4	42.6	0.8	7.0	17.1	9.3	7.7	1.2	2.8	88.6
611	Blina	Kimberley	Dillinger	ccam04611	2.46	3 × 3	9	43.3	0.9	8.5	17.4	8.4	5.7	1.6	1.8	87.5
611	Blinker_Hill	Kimberley	Dillinger	ccam05611	2.54	3 × 3	9	44.5	0.8	7.4	17.8	10.5	4.6	1.4	2.7	89.8
612	Windjana	Kimberley	Dillinger	ccam03612	2.43	5 × 5	25	44.7	0.9	7.4	18.0	9.6	4.8	1.3	2.9	89.6
618	Hawk	Kimberley	Dillinger	ccam02618	2.50	1 × 5	5	46.4	0.9	9.9	17.7	7.2	5.7	1.3	2.7	91.8
625	Windjana_drill_Hole_RMI	Kimberley	Dillinger	ccam03625	2.42	10 × 1	10	42.7	0.8	7.3	18.9	9.7	4.6	1.2	2.6	87.8
628	Yarrada	Kimberley	Dillinger	ccam03628	3.17	5 × 1	5	45.5	0.9	8.2	18.3	10.6	4.3	2.0	3.0	92.8
628	Dillinger	Kimberley	Dillinger	ccam04628	4.70	3 × 3	9	52.0	0.8	12.3	15.9	10.3	6.0	1.6	5.7	104.6
615	Mahoney	Kimberley	Mount Remarkable	ccam02615	5.06	1 × 5	5	48.5	0.8	11.2	17.5	8.5	6.5	1.6	5.3	99.9
625	San_Sou	Kimberley	Mount Remarkable	ccam05625	5.24	1 × 10	9	46.3	0.8	11.8	20.8	8.1	5.7	1.9	5.6	101.2
628	Mahoney_2	Kimberley	Mount Remarkable	ccam05628	5.08	1 × 5	5	47.0	0.8	10.7	18.8	8.9	5.7	1.7	4.8	98.5
618	Beagle	Kimberley	Beagle	ccam01618	4.00	4 × 4	16	44.3	1.3	10.0	20.6	8.7	4.6	2.5	1.6	93.5
							RMSE	*5.1*	*0.5*	*3.4*	*4.2*	*2.3*	*1.8*	*0.6*	*1.1*	*8.2*

[a]Their associated stratigraphic unit/member, sequence ID, distance of observation, observation type, number of points, and average chemical composition in major elements (in wt %) are indicated. The chemical composition of each point of each target is available on the PDS website (http://pds-geosciences.wustl.edu/missions/msl/chemcam.htm). ChemCam points on fracture-fill materials, soils, and drill tailings are not taken into account. Points with < 5e13 photons are also excluded. RMSE is the root-mean-square error of prediction and corresponds to the statistical accuracy of the method as obtained from terrestrial samples of known composition. The RMSE shown is the average accuracy of all targets.

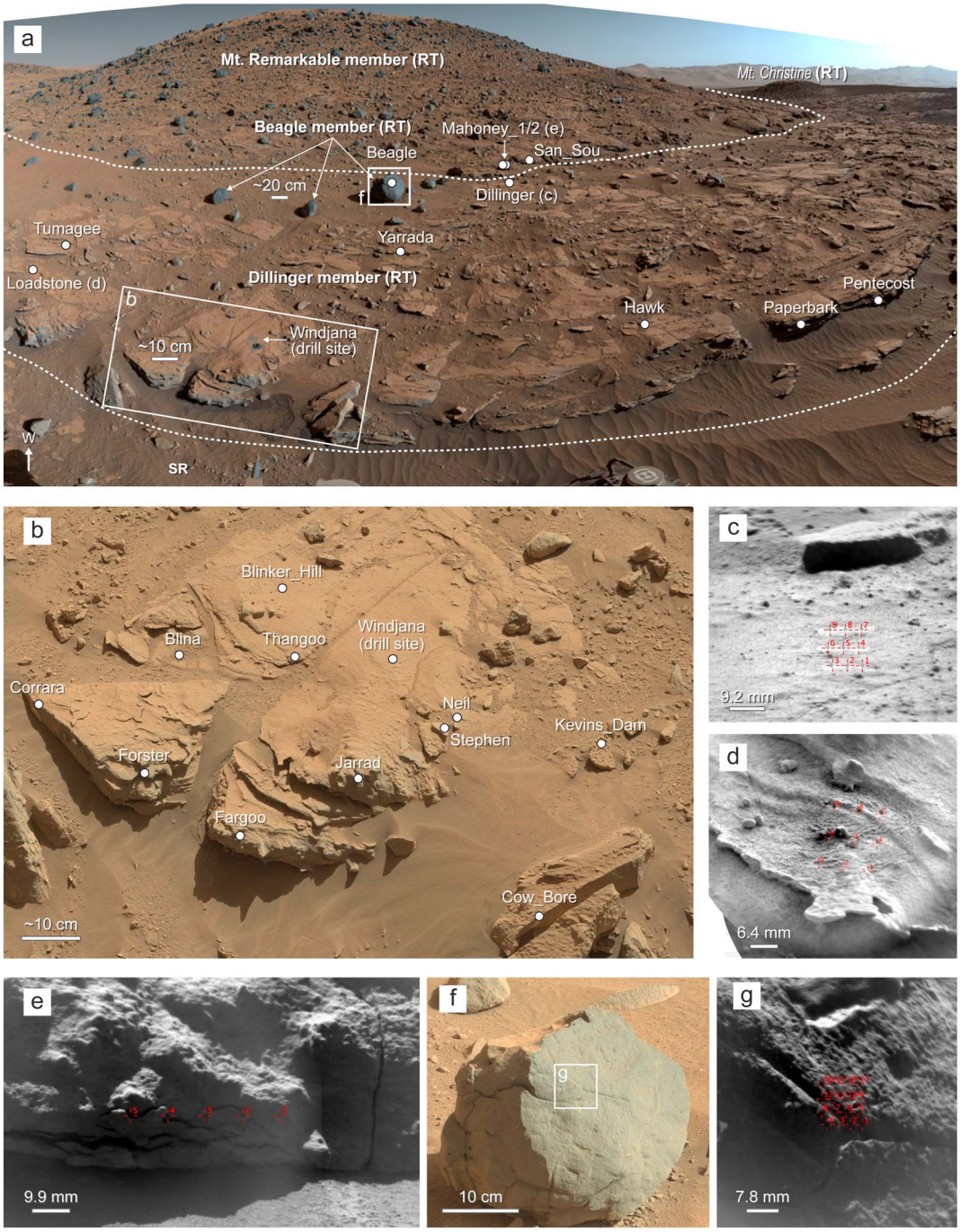

Figure 5. Facies of the uppermost members of the Kimberley formation: the Dillinger, Mount Remarkable, and Beagle members. (a) Mastcam panorama (mcam02652.0000a.mt_remarkable_180_10x8_L0) of Mount Remarkable. ChemCam targets are indicated (white dots) in Figures 5a and b. Tumagee, Loadstone, Stephen, and Neil are ChemCam targets on fracture fills. (b) Mosaic of Mastcam images (mcam02569.0000a.workspace_stereo_5x5_L0_R0) of the Windjana drill site (before the drill). (c) ChemCam RMI images of Dillinger (RMI images: CR0_453243050PRC_F0311330CCAM04628L1 and CR0_453243910PRC_F0311330CCAM04628L1). (d) ChemCam RMI images of Loadstone located on fracture-filling material (RMI images: CR0_453168065PRC_F0311330CCAM04625L1 and CR0_453169158PRC_F0311330CCAM04625L1). (e) ChemCam RMI images of Mahoney_2 (RMI images: CR0_453244134PRC_F0311330CCAM05628L1 and CR0_453244598PRC_F0311330 CCAM05628M1). (f) Mastcam image (0620MR0026530010401474E02_DXXX) of Beagle. (g) ChemCam RMI images of Beagle (RMI images: CR0_452355898EDR_F0311330CCAM01618M1, CR0_452356867EDR_F0311330CCAM01618M1, and CR0_452357634EDR_F0311330CCAM01618M1). ChemCam LIBS points are indicated (red) in Figure 5c-e and g.

Table 2. Average Composition in Major Elements in Oxide Weight Percent of the Potassic Sedimentary Rocks According to Their Geological Unit/Member[a]

Outcrop/Formation	Unit/Member	# of Targets	# of Points	SiO_2	RMSE	SD	TiO_2	RMSE	SD	Al_2O_3	RMSE	SD	FeO_T	RMSE	SD	MgO	RMSE	SD	CaO	RMSE	SD	Na_2O	RMSE	SD	K_2O	RMSE	SD	Total	SD	K_2O/Na_2O	SD
Cooperstown	Pine_Plains	3	48	**44.4**	5.1	3.1	**1.3**	0.6	0.3	**10.7**	3.5	3.8	**21.6**	4.4	2.4	**7.7**	2.2	2.9	**5.1**	1.7	1.5	**2.4**	0.6	0.4	**1.4**	0.9	0.7	**94.4**	5.3	**0.6**	0.29
Cooperstown	Rensselaer	3	21	**42.2**	5.2	1.7	**1.1**	0.5	0.2	**8.6**	3.4	2.0	**21.6**	4.4	1.4	**8.1**	2.3	1.8	**4.7**	1.6	1.3	**2.0**	0.6	0.3	**1.1**	0.9	0.3	**89.4**	3.4	**0.6**	0.18
Kimberley	Point_Coulomb	1	5	**47.2**	5.2	7.7	**0.8**	0.4	0.3	**15.9**	3.6	4.0	**21.3**	4.1	9.8	**2.4**	1.6	0.8	**2.5**	1.2	2.4	**4.3**	0.8	2.0	**1.9**	1.0	1.3	**96.5**	3.4	**0.4**	0.34
Kimberley	Liga (all locations)	15	125	**45.6**	5.1	5.4	**0.8**	0.4	0.2	**10.1**	3.5	3.7	**20.8**	4.1	8.0	**7.4**	2.2	3.4	**5.7**	1.9	2.3	**2.4**	0.6	1.0	**2.2**	1.1	1.7	**95.1**	4.8	**1.0**	0.87
Kimberley	Liga—northern Kimberley	5	44	**43.1**	5.3	5.4	**0.9**	0.5	0.2	**10.3**	3.5	3.9	**26.5**	4.7	8.6	**5.8**	2.0	2.5	**5.3**	1.8	1.9	**2.6**	0.7	1.3	**2.2**	1.1	1.2	**96.6**	5.5	**0.9**	0.66
Kimberley	Liga—eastern Kimberley	4	39	**46.2**	5.1	4.0	**0.8**	0.4	0.1	**10.8**	3.5	2.9	**19.8**	4.1	4.8	**7.1**	2.2	2.7	**5.9**	1.9	1.6	**2.4**	0.6	0.5	**2.0**	1.0	1.8	**95.0**	3.7	**0.9**	0.88
Kimberley	Liga—southern Kimberley	4	24	**47.6**	5.1	4.9	**0.8**	0.4	0.2	**8.4**	3.3	4.0	**14.9**	3.4	4.6	**10.9**	2.7	3.6	**6.0**	1.9	3.2	**2.5**	0.6	1.0	**1.9**	1.0	1.2	**92.9**	4.2	**0.8**	0.64
Kimberley	Liga—south of Kimberley	2	18	**47.8**	5.1	6.1	**0.7**	0.4	0.2	**10.2**	3.5	4.0	**16.9**	3.7	6.6	**7.0**	2.2	3.2	**6.1**	1.9	3.1	**2.2**	0.6	0.9	**3.3**	1.2	2.7	**94.3**	4.9	**1.7**	1.56
Kimberley	Square_Top	6	68	**42.0**	5.3	2.3	**0.9**	0.5	0.1	**8.3**	3.4	1.7	**24.5**	4.6	4.4	**7.5**	2.2	2.5	**5.7**	1.9	1.4	**1.9**	0.6	0.3	**2.2**	1.1	0.8	**92.9**	6.0	**1.2**	0.47
Kimberley	Dillinger	17	154	**44.9**	5.1	3.1	**0.9**	0.5	0.1	**8.5**	3.4	1.5	**18.5**	4.0	1.8	**9.2**	2.5	1.5	**5.5**	1.8	2.6	**1.5**	0.6	0.5	**3.3**	1.2	1.0	**92.3**	4.6	**2.4**	1.06
Kimberley	Mount Remarkable	3	19	**47.1**	5.0	1.5	**0.8**	0.5	0.1	**11.4**	3.5	1.0	**19.4**	4.1	2.1	**8.4**	2.3	0.9	**5.9**	1.9	1.3	**1.7**	0.6	0.2	**5.3**	1.4	0.7	**100.1**	2.1	**3.1**	0.59
Kimberley	Beagle	1	16	**44.3**	5.1	2.3	**1.3**	0.6	0.3	**10.0**	3.5	2.8	**20.6**	4.3	2.6	**8.7**	2.4	2.1	**4.6**	1.6	1.7	**2.5**	0.7	1.3	**1.6**	1.1	0.4	**93.5**	2.1	**0.7**	0.40
Yellowknife Bay	Sheepbed		482	**47.0**		2.1	**1.0**		0.1	**10.1**		1.5	**19.6**		0.9	**9.0**		2.1	**5.5**		1.4	**2.9**		0.4	**0.5**		0.2	**95.7**	2.9	**0.2**	0.1

[a]Average composition of the reference target Sheepbed (recalculated with new calibration compared to data used in *Mangold et al.* [2015]) and average K_2O/Na_2O ratio are indicated. RMSE and standard deviation (SD) around the average values are also shown.

The Liga member is a poorly sorted, planar-bedded, granule conglomerate and forms a few centimeter thick beds (Figures 3b, 4c, and 4e–4i). This member was analyzed by ChemCam in four sites at Kimberley, i.e., the northern site (Figures 4c and 4e), the eastern site (Figures 4f and 4i), the southern site (Figures 4f and 4h), and the site south of Kimberley (Figures 4f and 4g), which provides sufficient data to investigate the chemical variability within a stratigraphic member according to geographic location (Figure 3a). The targets belonging to each site are listed in Table 1.

The Liga member is overlain by the Square Top member, which primarily consists of south dipping decimeter thick bedsets of a very coarse sandstone that is mostly planar laminated and interbedded with thinner sandstone (Figures 4c and 4d). This series of erosion-resistant bedsets form distinct ridges, thus giving it its distinct appearance from orbit that inspired its name as the Striated unit. The Square Top member is estimated to be about 1 m thick [*Stack et al.*, 2016]. It has been analyzed by ChemCam in the northern Kimberley only.

The Dillinger member that overlies the Square Top member was investigated in detail at its outcrops in the southeastern Kimberley, at the foot of Mount Remarkable (Figures 5a–5d). The stratigraphic contact between the two members corresponds to a north dipping truncation surface [*Gupta et al.*, 2014]. The Dillinger member corresponds to a decimeter scale cross-bedded medium to fine sandstone of around half a meter in thickness [*Stack et al.*, 2016]. It is crosscut by fracture fills which are more resistant to erosion than surrounding host rock (Figure 5d). The fracture fills crosscut stratification with low angles or are parallel to bedding planes [*Lanza et al.*, 2015]. Analyses of the ChemCam instrument and APXS analyses reveal that those fracture fills are enriched in Mn [*Lanza et al.*, 2015]. Beyond numerous ChemCam and contact science observations, this sandstone has been drilled at a site named Windjana (Figures 5a and 5b), and material from it was delivered to the Chemistry and Mineralogy X-ray diffraction (CheMin) and Sample Analysis at Mars (SAM) Instrument Suite for mineralogical and volatile component analyses.

The Mount Remarkable member corresponds to massive coarse sandstone (Figures 3b, 5a, and 5e). It is associated with Mount Remarkable itself, which likely corresponds to a remnant butte of a former more extensive unit that likely included Mount Christine and Mount Joseph.

The Beagle member consists of boulders of sandstone of unknown grain size encountered on Mount Remarkable and at its foot (Figures 3b, 5a, 5f, and 5g). They likely correspond to erosional remnants of a unit stratigraphically above the Mount Remarkable member (Figure 3).

4. Chemistry

4.1. Potassic Sedimentary Rocks

The composition in major, minor, and trace elements of the sedimentary rocks of Cooperstown and Kimberley derived by ChemCam is reported in Tables 1–4 and described in Figures 6–8. They have a basaltic-like composition and primarily differ in composition from the sedimentary rocks previously encountered by Curiosity by their significantly higher content of K_2O (Tables 2 and Figure 6a). The mean K_2O content of these rocks is ~2.5 wt %, which is about 5 times higher than the mean K_2O content of the Sheepbed member in Yellowknife Bay (Table 2 and Figure 6c). In order to classify the chemical composition of rocks encountered along the traverse in Gale Crater, we used elemental enrichment and/or depletion relative to average Martian crust [*Taylor and McLennan*, 2009], as suggested for the classification of sedimentary rocks by Curiosity [*Schmidt et al*., 2015, Figures 7a and 7b]. Most of Cooperstown and Kimberley rocks are thus potassic, having a K_2O content >1 wt %, which is twice as much K_2O as the average Martian crust (Figure 7b).

Some chemical variations occur between the different units/members of each outcrop/formation that are suggestive of different chemical components (Figures 6 and 7). The Cooperstown outcrop and Kimberley formation can be divided into four major chemical groups, which are, in order of increasing average K_2O content the Cooperstown outcrop & the Beagle member (average $K_2O = 1.3$ wt %), the Point Coulomb member (average $K_2O = 1.9$ wt %), the Liga & Square Top members (average $K_2O = 2.2$ wt %), and the Dillinger & Mount Remarkable members (average $K_2O = 4.3$ wt %).

4.2. Cooperstown Outcrop & Beagle Member

The Cooperstown outcrop includes the Pine Plains and the Rensselaer units. Compared to the other groups, the Cooperstown outcrop has on average: high TiO_2 (1.1–1.3 wt %), MgO (7.7–8.1 wt %), and MnO (0.8–0.9 wt %); moderate Al_2O_3 (8.6–10.7 wt %), FeO_T (21.6 wt %), CaO (4.7–5.1 wt %), and Na_2O (2.0–2.4 wt %); moderate to low SiO_2 (42.2–44.4 wt %); and the lowest K_2O (1.1–1.4 wt %) (Tables 2–4 and Figures 6a and 8a). In terms of minor and trace elements (Table 3 and Figures 8a and 8b), this group contains moderate Li, low Sr and Rb, and almost no F nor Zn. A relatively high H signal is detected in this outcrop.

The Beagle member, which is not associated with the Cooperstown outcrop but rather with the Kimberley formation, shows chemical compositions very close to those of the Cooperstown rocks. As a result, we classified the Cooperstown outcrop and the Beagle member in the same chemical group.

Abundances of FeO_T, MgO, CaO, and TiO_2, and the presence of less potassic compositions relative to the average Martian crust (which has $K_2O < 1$ wt %), suggest the presence of more mafic minerals such as olivine and pyroxenes in this group. Abundances of Al_2O_3, CaO, and Na_2O also indicate the presence of plagioclase (Figures 7g and 7h). This group has a fairly high average K_2O/Na_2O ratio, at about 0.6. There are positive correlations among abundances of K_2O, Na_2O, and Al_2O_3. One LIBS point of the Pine Plains unit has an abundance of K_2O reaching 2.7 wt %, with $K_2O/Na_2O \approx 0.8$, and its Al_2O_3 abundance reaching 18.6 wt % (Pine Plains unit, Cobleskill target, point #20, gray arrows in Figures 7b, 7c, and 7f), suggesting the presence of K-bearing minerals such as alkali feldspars in the mixture. Abundances of K_2O and MgO are inversely correlated, indicating that micas like biotite, or clays like illite are unlikely to be among the K-bearing minerals (Figure 7e). Abundances in Al_2O_3 are too low for the only K carrier to be muscovite (Table 1).

4.3. Point Coulomb Member

The Point Coulomb member is documented only by five ChemCam LIBS points on the target JumJum. Hence, no chemical trends can be inferred for the entire member, especially considering the fact that it corresponds to breccio-conglomerate for which chemical diversity might be expected. Compared to the other groups, the JumJum target of the Point Coulomb member has high SiO_2, Al_2O_3, FeO_T, and Na_2O, moderate K_2O, and low MgO, CaO, MnO and TiO_2 (Figure 6a). It has the highest signal in H, high Li, moderate Sr, and low Rb (Figures 8a and 8b). Positive correlations among abundances of Al_2O_3, Na_2O, and K_2O suggest the presence of alkali feldspar (Figures 7b, 7c, 7f, and 7h). One of the LIBS points is very close to the composition of anorthoclase feldspar: $SiO_2 \approx 58.5$ wt %, $Al_2O_3 \approx 20.3$ wt %, $Na_2O \approx 7.6$ wt %, $K_2O \approx 4.0$ wt %, and almost no MgO and CaO (point #5, purple arrows in Figure 7). Other chemical components for this target may be Fe-rich phases, likely including hydroxylated or hydrated phases such as Fe-oxides, Fe-hydroxide/

Table 3. Average Abundance in MnO, H, F, Zn, and in Minor Elements of the Potassic Sedimentary Rocks According to Their Stratigraphic Unit/Member[a]

Outcrop/Formation	Unit/Member	MnO (wt %)	SD	H SBR (arbitrary units)	SD	F (wt %)	SD	Zn (wt %)	SD	Li (ppm)	SD	Rb (ppm)	SD	Sr (ppm)	SD
Cooperstown	Pine Plains	**0.9**	1.8	**0.4**	0.1	**0.01**	0.04	-	-	**21**	5	**34**	42	**270**	91
Cooperstown	Rensselaer	**0.8**	0.4	**0.4**	0.1	-	-	-	-	**24**	11	**55**	54	**282**	86
Kimberley	Point_Coulomb	**0.4**	0.2	**0.6**	0.1	-	-	-	-	**33**	28	**45**	55	**311**	134
Kimberley	Liga (all locations)	**0.6**	0.8	**0.4**	0.2	**0.01**	0.06	**0.01**	0.08	**18**	14	**113**	8	**296**	194
Kimberley	Liga—northern Kimberley	**1.1**	1.3	**0.3**	0.2	**0.02**	0.07	**0.01**	0.07	**11**	12	**108**	97	**327**	172
Kimberley	Liga—eastern Kimberley	**0.6**	0.4	**0.3**	0.3	-	0.03	**0.01**	0.08	**19**	17	**108**	73	**291**	131
Kimberley	Liga—southern Kimberley	**0.1**	0.1	**0.6**	0.2	**0.01**	0.08	-	-	**25**	6	**97**	45	**246**	231
Kimberley	Liga—south of Kimberley	**0.4**	0.3	**0.3**	0.1	**0.02**	0.09	**0.02**	0.11	**19**	14	**156**	94	**304**	279
Kimberley	Square_Top	**1.0**	0.4	**0.2**	0.1	**0.02**	0.10	-	-	**9**	3	**133**	60	**323**	116
Kimberley	Dillinger	**0.5**	0.3	**0.2**	0.3	**0.03**	0.10	**0.14**	0.55	**17**	10	**135**	48	**442**	106
Kimberley	Mount Remarkable	**0.7**	0.3	**0.1**	0.1	**0.07**	0.11	**0.12**	0.26	**35**	6	**217**	44	**372**	112
Kimberley	Beagle	**1.2**	0.9	**0.3**	0.2	-	-	-	-	**27**	8	**30**	29	**311**	123

[a]Standard deviation around the average values are also indicated. For some elements such as F and Zn, the standard deviation values are higher than those of mean abundances. This is due to the fact that these elements are detected for only a few ChemCam LIBS points.

oxyhydroxide, and Fe-phyllosilicates because most of the LIBS points show high FeO_T and H abundances (Figures 7a and 8a).

4.4. Liga & Square Top Members

The Liga & Square Top members have the same average K_2O content, which is ca. 2.2 wt % (Figure 6a). Compared to the other groups, the Liga member has moderate average abundances for all major elements (Figures 6a and 8a). In detail, it shows a strong variability in chemistry, with the most extreme compositions associated with those that are either most enriched or most depleted in Fe, Si, and alkali elements, which implies that several chemical components are present in this group (Figures 6b and 7). Among Liga targets, chemical variations vary by geographic location. The northern targets of the Liga member show lower SiO_2 and higher FeO_T than the average composition of the Liga member (Figure 6b). The southern targets have lower Al_2O_3, FeO_T, and higher MgO. Targets at the south of Kimberley have the highest K_2O content of all groups, with K_2O reaching up to 11.4 wt % for a LIBS point on the Kalumburo target. This point likely corresponds to a nearly pure K-feldspar such as sanidine, with $SiO_2 \approx 63.1$ wt %, $Al_2O_3 \approx 19.7$ wt %, and $Na_2O \approx 1.4$ wt % (point #3, green arrows in Figure 7). Some points with the highest Al_2O_3 and Na_2O contents as well as fairly high K_2O contents likely also correspond to alkali feldspars (Figures 7b, 7c, and 7h). No negative correlation occurs between MgO and K_2O, which suggests that some of the K-bearing phases contain Mg, and may correspond to clay minerals or micas, e.g., illite and biotite (Figure 7e). The occurrence of F, often present in micas in terrestrial strata, is consistent with their presence in the Liga member (Figure 8a). Some analyses show high Al_2O_3, Na_2O, and high CaO that likely reflect the occurrence of plagioclase (Figures 7g and 7h). High abundances of FeO_T are partly due to the presence of other mafic silicate minerals but likely also correspond to Fe-oxides, Fe-oxyhydroxides, and/or Fe-phyllosilicates in the Liga member (Figure 7a). The Liga member has on average moderate Rb and Sr, which is consistent with the presence of K-bearing minerals, plagioclase, and other mafic minerals in the mixture.

The Square Top member is more homogeneous in its chemical composition than the Liga member (Figure 7). The average composition of the Square Top member is similar to the Fe-rich, potassic compositions of the Liga member, and especially to those of the northern Kimberley (Figure 7a). Since the Square Top member was analyzed at the same outcrop as the northern Liga member, their close composition may be due to similar, likely Fe-rich local

Table 4. Summary of the Chemical Composition Inferred for Each Unit/Member From ChemCam Data and the Corresponding Expected Mineralogy[a]

Outcrop/Formation	Unit/Member	Facies	Chemical Group	Relative Abundance in Major Elements	Relative Abundance in Minor Elements	Expected Mineralogy
Cooperstown	Pine_Plains Rensselaer	Massive fine sandstone Massive coarse sandstone	Cooperstown outcrop & Beagle member	•High TiO_2, MgO, and Mn •Moderate Al_2O_3, FeO_T, CaO, and Na_2O •Moderate to low SiO_2 •Lowest K_2O	•High H signal. •Moderate Li •Low Sr and Rb •Almost no F, nor Zn.	•Mafic minerals (olivine, pyroxenes, plagioclase). •Alkali feldspars.
Kimberley	Point_Coulomb	Pebble conglomerate	Point Coulomb member	•High SiO_2, Al_2O_3, FeO_T, and Na_2O. •Moderate K_2O. •Low, MgO, CaO, Mn and TiO_2.	•Highest signal in H. High Li. •Moderate Sr. •Low Rb. •No F, nor Zn.	•Alkali feldspars (anorthoclase). •Fe-oxides, Fe-hydroxide/oxyhydroxide, and Fe-phyllosilicates.
Kimberley	Liga (all locations) Liga - northern Kimberley Liga - eastern Kimberley Liga - southern Kimberley Liga - south of Kimberley	Planar-bedded granule conglomerate	Liga &Square Top members	•Moderate average abundances in all major elements. •Higher FeO_T Lower SiO_2 •Higher Al_2O_3. •Higher MgO. •Lower Al_2O_3, FeO_T. •Higher K_2O.	•High H signal. •Moderate Li, Rb, and Sr. •Low F, and Zn.	•Mafic minerals (olivine, pyroxenes, plagioclase). •Alkali feldspars (including sanidine), K-phyllosilicates. •Fe-oxides, Fe-hydroxide/oxyhydroxide, and Fe-phyllosilicates.
	Square_Top	South dipping medium to very coarse sandstone		•Higher FeO_T and K_2O/Na_2O ratio than Liga	•Low H signal. •Higher F, Rb, and Sr than Liga. •Lowest Li. •No Zn.	
Kimberley	Dillinger Mount Remarkable	Cross-stratified medium to fine sandstone Massive coarse sandstone	Dillinger & Mount Remarkable members	•High MgO. •Moderate CaO and Mn. •Low FeO_T, TiO_2, and Na_2O.	•Low H signal. •High F, Zn, Rb, and Sr. •Moderate to high Li.	•Mafic minerals (olivine, pyroxenes, plagioclase). •Alkali feldspars (including sanidine), K-phyllosilicates.
Kimberley	Beagle	Float blocks	Cooperstown outcrop & Beagle member	•High TiO2, MgO, and Mn •Moderate Al2O3, FeOT, CaO, and Na2O •Moderate to low SiO2 •Lowest K2O	•High H signal. •Moderate Li and Sr. •Low Rb. •No F, nor Zn.	•Mafic minerals (olivine, pyroxenes, plagioclase). •Alkali feldspars.

[a]Abundances in major and minor elements are indicated as high, moderate or low compared with the other chemical groups, and with the Liga (all locations) for the different analyzed locations of the Liga member.

components. On average, the Square Top member has a slightly higher K_2O/Na_2O ratio than that of the Liga member, i.e., about 1.2 against 1.0, respectively, suggesting a higher concentration of K-bearing minerals in the mixture. In terms of minor and trace elements, the Square Top member has a higher abundance of F, Rb, and Sr than the Liga member. It has the lowest content of Li of all chemical groups and no detectable Zn.

4.5. Dillinger & Mount Remarkable Members

Compared to the other members, the Dillinger & Mount Remarkable members have the highest average abundances of K_2O, which are respectively 3.3 wt % and 5.3 wt %. This group also averages high MgO (8.4–9.2 wt %), moderate to high SiO_2 (44.9–47.1 wt %), low to moderate Al_2O_3 (8.5–11.4 wt %), moderate CaO (5.5–5.9 wt %) and MnO (0.5–0.7 wt %), low FeO_T (18.5–19.4 wt %), TiO_2 (0.8–0.9 wt %), and Na_2O (1.5–1.7 wt %) compared to the other chemical groups (Figure 6a). In terms of minor, trace and volatile elements, the Dillinger & Mount Remarkable members have high abundances of F, Zn, Rb, and Sr; high to moderate abundances of Li; and low abundance of H (Figures 8a and 8b). Interestingly, there is a strong positive correlation between abundances of Rb and K, with a coefficient of determination $R^2 > 0.6$ (Figure 8c). Rb is a lithophile element that can substitute

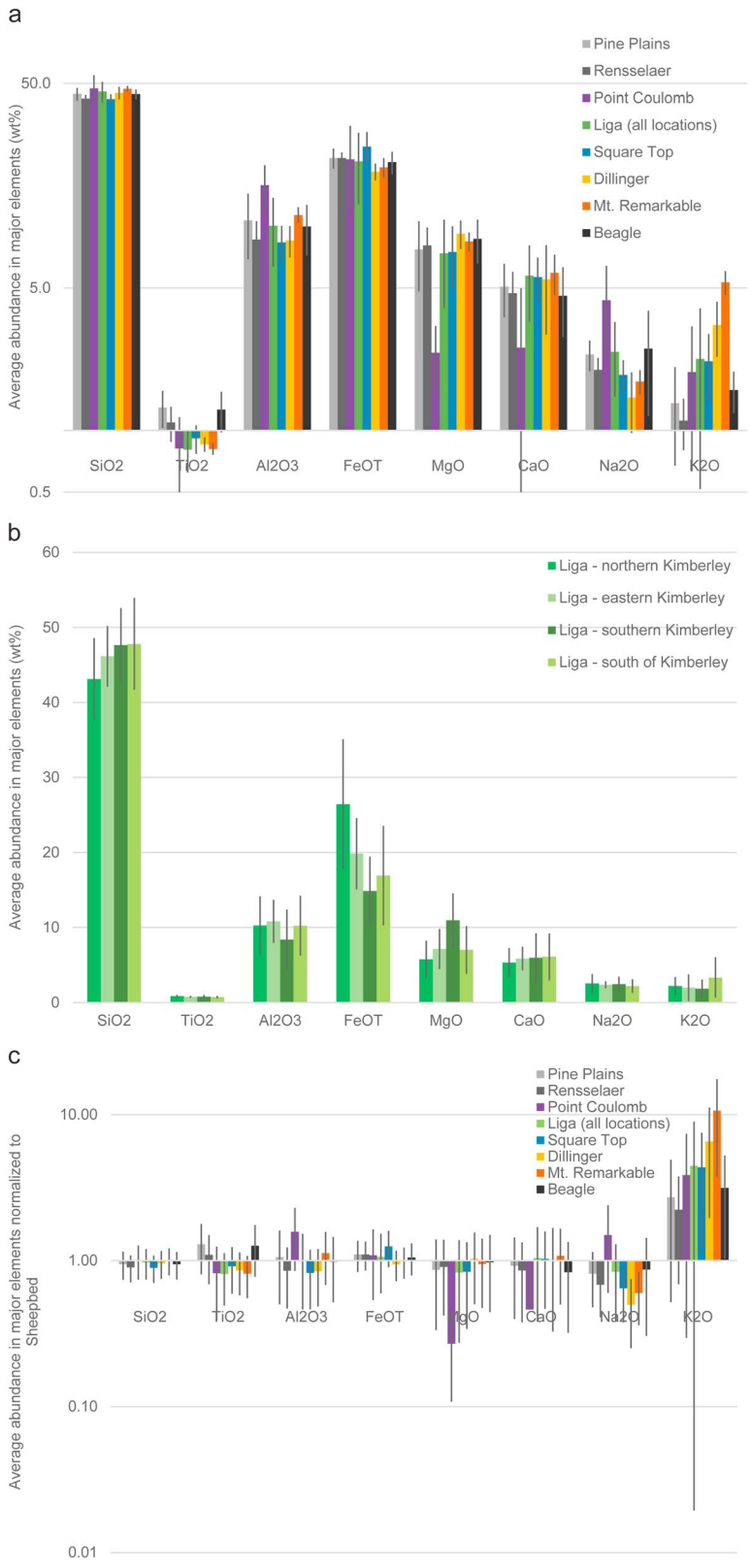

Figure 6. Average composition in major elements of the potassic sedimentary rocks analyzed by ChemCam. Error bars (black bars) are standard deviation of the compositions and primarily reflect heterogeneity within each unit/member. (a) Average composition of each unit/member. (b) Average composition of the Liga member for each location. (c) Average composition of each unit/member normalized to Sheepbed (YKB).

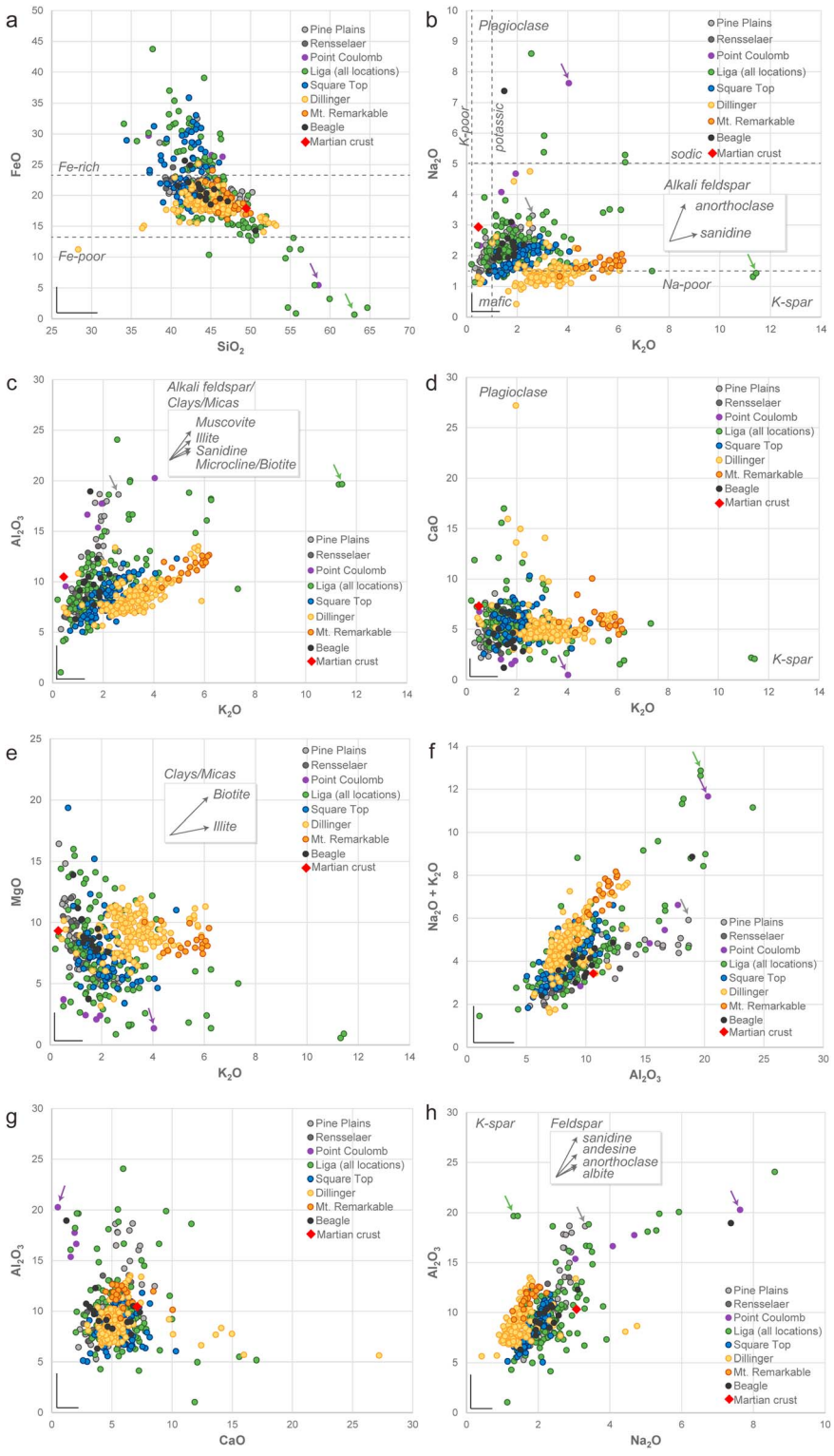

Figure 7. Plots of the major element composition of the potassic sedimentary rocks analyzed by ChemCam. Each ChemCam point for each unit/member is shown. Composition of the average Martian crust is indicated for reference, as well as common ratios for feldspar, clays and micas represented by black arrows. Abundances are in weight percent. Black lines in the lower left corner of each plot indicate RMSE for each oxide. Colored arrows refer to ChemCam LIBS points discussed in the text. (a) FeO versus SiO_2. Dotted lines show Fe-rich and Fe-poor compositions relative to average Martian crust according to the chemical classification of sedimentary rocks at Gale Crater [*Schmidt et al.*, 2015]. (b) Na_2O versus K_2O. Purple arrow denotes a ChemCam point that is consistent with pure anorthoclase feldspar, see text. Dotted lines show potassic, K-poor, sodic, and Na-poor compositions relative to average Martian crust according to the chemical classification of sedimentary rocks at Gale Crater [*Schmidt et al.*, 2015]. (c) Al_2O_3 versus K_2O. (d) CaO versus K_2O. (e) MgO versus K_2O. (f) $Na_2O + K_2O$ versus Al_2O_3. (g) Al_2O_3 versus CaO. (h) Al_2O_3 versus Na_2O.

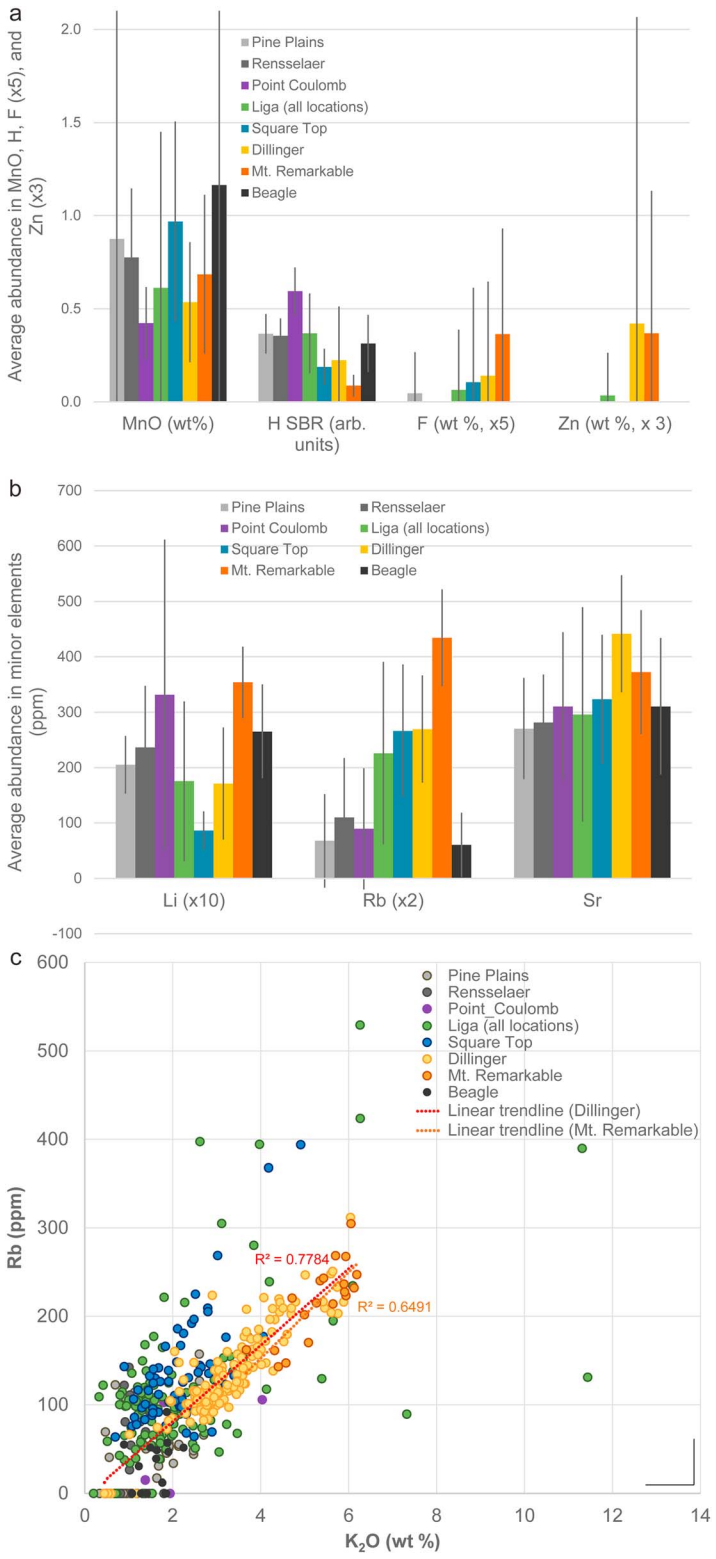

Figure 8. Average abundance in MnO, H, F, Zn, and in other minor and trace elements of the potassic sedimentary rocks analyzed by ChemCam. Error bars (black bars) are standard deviation of the compositions and primarily reflect heterogeneity within each unit/member. (a) Average abundance in MnO, H, F, and ZnO for each unit/member. (b) Average composition in Li, Rb, and Sr for each unit/member. (c) Rb versus K_2O for each unit/member. Linear trendlines and the corresponding coefficient of determination are indicated for Dillinger and Mount Remarkable members. Black lines in the lower right corner of the plot indicate RMSE for Rb and K_2O.

for K, indicating that both elements are likely present in the same K-bearing minerals. During the first 1000 sols, 12 targets on Mars were detected with high ZnO content ranging from 1.0 wt % to a maximum of 8.4 wt % [*Lasue et al.*, 2016]. Almost all those Zn-enriched targets are localized in the Dillinger and Mount Remarkable members [*Lasue et al.*, 2016].

Rocks of the Dillinger member are very rich in potassium; some LIBS analyses reach $K_2O \approx 6$ wt %, and all have $K_2O/Na_2O \approx 2.4$. This implies that the group contains a far greater proportion of K-bearing phases than any other at Cooperstown and Kimberley (and in fact of all other rocks analyzed by Curiosity). These K-bearing phases could include alkali feldspar (especially high K-feldspar like sanidine), illite, biotite, and possibly K-rich amorphous material. The presence of K-bearing phyllosilicates is inferred by the fact that there is a weak correlation between MgO and K_2O abundances, suggesting that Mg and K occur partly in common mineral phases. No LIBS point displays any notably elevated Al_2O_3 abundance that would suggest the presence of muscovite.

The K_2O/Na_2O ratio of the Mount Remarkable member reaches about 3.1. Its composition is homogeneous and is similar to that of the most K-enriched targets of the Dillinger member. The lower signal in H in the Mount Remarkable member than in the Dillinger member may suggest a lower concentration in phyllosilicates in the Mount Remarkable member than that in the Dillinger member. As a result, there is an increase in average K_2O abundances and K_2O/Na_2O ratios between the different groups, implying an increase in concentration of K-bearing phases.

The chemical composition inferred for each member from ChemCam data as well as the expected mineralogical composition is summarized in Table 4.

5. Discussion

5.1. Constraints From CheMin Results

The Dillinger member has been sampled at the Windjana drill site. Analyses of the CheMin X-ray diffraction instrument reveal that the Windjana sample contains sanidine (21% by weight, $\sim Or_{95}$); augite (20%, $\sim Wo_{37}En_{42}Fs_{21}$); magnetite (12%); pigeonite (11%, $\sim Wo_{02}En_{65}Fs_{33}$); olivine (5%, $\sim Fo_{60}$); plagioclase (3%, $\sim An_{40}$); amorphous and clay material (25%); possible percent-level concentrations of fluorapatite, ilmenite, hematite, pyrrhotite, akaganeite, anhydrite, kaolinite, and bassanite; and possibly a trace proportion of illite [*Treiman et al.*, 2016]. Diffraction from the clay material are consistent with those of a collapsed ferromagnesian smectite [*Vaniman et al.*, 2014], which is also consistent with mass balance calculations using APXS chemical data [*Treiman et al.*, 2016]. The amorphous material is inferred to contain low K contents [*Dehouck and McLennan*, 2015] to no K (within uncertainty) [*Treiman et al.*, 2016] and is likely to be mostly ferrihydrite [*Treiman et al.*, 2016]. No amphiboles, micas, chlorites, Fe/Mg sulfates, or Mn-rich minerals were detected.

The ChemCam analyses suggest that the chemical composition of the Dillinger member is consistent with a mixture of mafic minerals and K-bearing phases including alkali feldspar such as sanidine, K-bearing phyllosilicates such as illite or biotite, and possibly K-rich components in the amorphous phase. CheMin results confirm the presence of alkali feldspar corresponding to nearly pure $KAlSi_3O_8$. Sanidine typically has a K_2O abundance of ~12.9 wt %. A mass balance calculation suggests that the occurrence of ~21 wt % of sanidine in the Dillinger member (as estimated at the Windjana drill site using CheMin) would account for ~2.7 wt % of K_2O. The Dillinger member has an average abundance of K_2O of 3.3 wt %, which confirms that additional K-bearing minerals are required in the mixture to account for the abundance of K_2O. CheMin results suggest the possible occurrence of illite, which indicates that a K-phyllosilicate is likely among the K-bearing minerals present in Dillinger. From our mass balance calculation, ~0.6 wt % of K_2O would be in the K-phyllosilicate phase, which would correspond to ~8.2 wt % of illite. Lack of K in the amorphous material inferred from CheMin results suggests that concentrations of K-rich phases in the amorphous material are likely limited. The F detected by ChemCam may occur in fluorapatite, illite, augite, and/or pigeonite (see *Forni et al.* [2015a–b] for more comprehensive discussion on F). No minerals with stoichiometric Mn were detected by CheMin, which is consistent with the suggestion, based on ChemCam data, that Mn may be present in the pyroxenes and olivine. The H detected by ChemCam is consistent with the presence of clays and ferrihydrite.

CheMin's detections of magnetite and ferrihydrite in the Dillinger member suggest that some of the Fe-rich phases and hydrated or hydroxylated phases likely present in the Point Coulomb member and the Liga &

Square Top members may also correspond to those minerals. As a result, the constraints from CheMin analyses of the Dillinger member indicate that the enrichment in K of these basaltic sedimentary rocks is mostly due to the presence of sanidine in the Dillinger member. A K-phyllosilicate likely also contributes to this enrichment. Various alkali feldspars and K-phyllosilicates may be present in the other members as summarized in Table 4.

5.2. Origins of the Enrichment in K

The sedimentary rocks at Cooperstown and Kimberley are the most enriched in K that have been encountered by Curiosity since the Bathurst Inlet outcrop in the YKB formation. Considering the Cooperstown outcrop and the Kimberley formation together, it appears that abundances of K increase gradually upward in the stratigraphic section (with the assumption that the Kimberley formation is stratigraphically above the Cooperstown series) [*Grotzinger et al*., 2015; *Stack et al*., 2016]. An exception concerns the uppermost member of the Kimberley formation, the Beagle member that has the same chemical composition than the Cooperstown outcrop, possibly suggesting that they share common source rocks and/or formation processes. Both diagenetic and detrital origins may be considered for this increase in K and are discussed below.

5.2.1. Diagenetic Origin of K Enrichment

All sedimentary rocks at Cooperstown and Kimberley appear rather well cemented. Alkali feldspar and K-phyllosilicate might have formed by diagenesis [e.g., *Ali and Turner*, 1982; *Bjorkum and Gjelsvik*, 1988]. However, several observations suggest that a diagenetic origin for those minerals is rather unlikely. CheMin results indicate the presence of easily altered minerals including olivine, plagioclase, and pyrrhotite in significant proportions (section 5.1), showing that diagenesis beyond extensive cementation of the Dillinger member was limited [*Treiman et al*., 2016]. Moreover, the chemical group with the most enrichment in K is the Dillinger and Mount Remarkable members. If the K-rich minerals were formed in situ by significant diagenesis, the Liga & Square Top members that are located stratigraphically below the Dillinger & Mount Remarkable members might be expected to also have rather similar enrichments in K. The presence of fracture fills in the Cooperstown outcrop and in the Dillinger member attests that postdepositional alteration occurred, although, at Cooperstown and Kimberley. The fracture fills in the Dillinger member are enriched in Mn, but this is not the case of the host rock, which has less than one eighth of the Mn as do the fracture fills. This suggests that the host rock was already cemented during this postdepositional alteration and consequently that the K-bearing minerals did not form during this alteration phase.

5.2.2. Detrital Origin of K Enrichment

A detrital origin is a second possible cause for the enrichment in K of these basaltic sedimentary rocks. The occurrence of different source rocks in various proportions may result in the mineralogical assemblages observed for each member. As discussed in *Treiman et al*. [2016], high abundances in sanidine and pigeonite in the Dillinger member alone argue in favor of at least two sources. They discuss the possibility that a potassic source rock of the Dillinger & Mount Remarkable members may correspond to a trachytic rock with $>40\%$ sanidine and $>25\%$ augite. Such alkaline K-feldspar-bearing materials have previously been encountered along the traverse on the hummocky plains and may correspond to igneous clasts and float rocks described in *Sautter et al*. [2015]. The rocks of the Dillinger member as well as the other potassic sedimentary rocks at Cooperstown and Kimberley may derive from the same sources as those igneous clasts and float rocks. *Treiman et al*. [2016] inferred that another source rock in the mixture may correspond to a shergottite-like basalt rich in pigeonite and olivine and with relatively little feldspar corresponding to the chemical component associated with more mafic minerals in the ChemCam analyses. The K-bearing minerals may have been transported by fluvial processes from different sources on Gale Crater's rim, resulting from different flow types and/or directions or watershed extent. The truncation surface between the Liga & Square Top members (Striated Unit) and the Dillinger & Mount Remarkable members (Rugged Unit), which have different attitude and dip angles may provide evidence of those different sources of sediment. Depositional models of the sediments at Kimberley [*Grotzinger et al*., 2015] are described in detail in *Gupta et al*. [2014]. In addition to the presence of potassic source rocks in the mixtures, physical sorting may have contributed to the observed enrichment in K [e.g., *Siebach et al*., 2015]. However, physical sorting typically tends to concentrate heavy mafic crystals and small crystals like micas in the finer fractions, leaving out coarser grains such as feldspars [*Kiminami and Fujii*, 2007; *Mangold et al*., 2011; *Fedo et al*., 2015]. Though the concentration of low-density crystals of alkali feldspar may have not been increased by sorting, small crystals of K-phyllosilicate may have been concentrated in the finest fractions of the Kimberley formation (apart from the Point Coulomb member which does not contain any).

To summarize, we suggest that the K-bearing minerals have primarily a detrital origin. They may have formed in the primary paragenesis or formed during predepositional alteration. Sediment deposition of different source rocks resulted in the observed mineralogical assemblages. Within the Liga & Square Top members and the Dillinger & Mount Remarkable members, which both have the highest average contents of K_2O and include K-phyllosilicate such as illite in addition to alkali feldspar in their K-bearing minerals, physical sorting may have also contributed to their enrichment in K.

Thus, although more complex provenance scenarios are certainly possible, it may be possible to explain the igneous mineralogy and geochemistry of these sedimentary rocks with as few as two major sources. One source component would include K-rich igneous rocks, such as those described by *Sautter et al*. [2015] and the second, a relatively low-alkali basaltic rock to provide pigeonite and other mafic minerals [*Treiman et al*., 2016]. In such a two component model, the most likely source of the K-phyllosilicates would be weathering or other aqueous alteration of the K-rich igneous rocks in the source terrain. Additional minor sources and/or processes would be required to explain some of the minor phases that are observed (e.g., hematite, anhydrite, and kaolinite).

5.3. Comparison With Other Potassic Sedimentary Rocks at Gale Crater

The potassic sedimentary rocks previously encountered during the mission all belong to the YKB formation and are associated with the uppermost Glenelg member [e.g., *Mangold et al*., 2015]. They occur at three outcrops which are Shaler, Rocknest, and Bathurst Inlet. Shaler was the first exposure of dipping beds observed on the mission, some 7 km northeast of the striated unit at Kimberley [*Grotzinger et al*., 2014]. Consisting of fine to coarse sandstones, these beds show a heterogeneous chemistry which is overall enriched in K relative to Sheepbed, but with an average abundance of $K_2O < 1$ wt % as measured by ChemCam [*Anderson et al*., 2015a] (revised calibration). The K_2O/Na_2O ratio is also lower than that of the Cooperstown and Kimberley rocks, suggesting a lower proportion of alkali feldspars in Shaler than in the Cooperstown and Kimberley rocks. The Rocknest outcrop has also a lower average abundance of K_2O than the Cooperstown and Kimberley rocks, i.e., $K_2O \sim 1.0$ wt %, but shows similar high abundances of FeO_T than the Square Top member and the northern Kimberley Liga member, with an average FeO_T of 26.3 wt % [*Blaney et al*., 2014]. The Bathurst Inlet outcrop corresponds to a group of thinly laminated fine-grained rocks that were fractured and modified by weathering [*Mangold et al*., 2015]. Previously classified with igneous rocks [*Schmidt et al*., 2014], their exact nature, whether volcaniclastic or sedimentary, is still uncertain [*Sautter et al*., 2013; *Mangold et al*., 2015]. The Bathurst Inlet outcrop shows the highest average K_2O abundance of the YKB formation, with $K_2O \sim 1.1$ wt % (average of five ChemCam LIBS points only), and a K_2O/Na_2O ratio of ~0.6 [*Mangold et al*., 2015]. Hence, it has a similar average K_2O abundance to that of the Rensselaer member and a similar K_2O/Na_2O ratio than that of the Cooperstown outcrop & Beagle member chemical group. If the Bathurst Inlet outcrop is indeed comprised of sedimentary rocks, then they may share common source rocks with those of the Cooperstown outcrop & Beagle member chemical group.

5.4. Further Evidence of an Alkali- and Silica-Rich Crust on Mars

It has been known since the 1980's that Mars is enriched in alkali elements [*Dreibus and Wänke*, 1985, 1987]. However, the 2001 Mars Odyssey Gamma Ray Spectrometer (GRS) data provide a global view of the Martian crust which would limit the overall distribution of high K rocks on Mars [e.g., *Taylor et al*., 2006]. The GRS data predict a moderate concentration of K in the region of Gale, ranging between 0.3 wt % and 0.4 wt % [*Taylor et al*., 2006; *Boynton et al*., 2007; *Gasnault et al*., 2010], suggesting that current and future landed missions may reveal further high K rocks unseen from orbit.

Over the last years, several findings have indeed revealed the occurrence of alkali- and silica-rich rocks in addition to the typical basaltic rocks on Mars. First, felsic igneous clasts and rocks analyzed with Curiosity along the traverse have compositions spanning from alkali basalt to trachyte and even mugearite [*Stolper et al*., 2013; *Sautter et al*., 2015]. Second, alkalic volcanism on Mars was predicted based on the mineralogy of the chassignite dunites [*Nekvasil et al*., 2007], and k-rich magmas were also predicted based on the mineralogy of the nakhlites [*Goodrich et al*., 2013]. Potassic igneous activity is discussed in further detail in *Treiman et al*. [2016]. The impact breccia Martian meteorite NWA7034/7533/7475 contains mafic and felsic clasts embedded in various impact melt rocks and a fine-grained matrix [*Humayun et al*., 2013; *Hewins and NWA 7533 Consortium*, 2014; *Wittmann et al*., 2015]. Some of the clasts have a monzonitic composition containing

up to 5.58 wt % K_2O [*Humayun et al.*, 2013]. Finally, recent orbital mineralogical analyses of the surface by near infrared spectroscopy using Compact Reconnaissance Imaging Spectrometer for Mars detected possible feldspar-rich materials in crater floors, rims, and peaks in the southern highlands of Mars [*Carter and Poulet*, 2013; *Wray et al.*, 2013; *Ding et al.*, 2015]. Taken together these observations suggest that silica-rich magmatic rocks may constitute a greater fraction of ancient Martian crust than previously thought (see *Sautter et al.* [2016] for further discussion).

6. Conclusions

The analysis of ChemCam data from Curiosity reveals the occurrence of potassic sedimentary rocks on the plains at the foot of Aeolis Mons in Gale Crater. They have an average abundance of K_2O that is more than 5 times higher than that of the average Martian crust. Encountered at two waypoints, namely, Cooperstown and Kimberley, those rocks form several meters thick sedimentary series of varied facies ranging between fine sandstone and conglomerate, interpreted to record an ancient fluvial, or fluvio-deltaic system in Gale Crater [*Grotzinger et al.*, 2015; *Gupta et al.*, 2014]. The combined analysis of ChemCam data with stratigraphic and geographic locations shows that the average abundance of K_2O generally increases upward through the stratigraphic section. Different chemical components are present in each member and point toward the presence of different mineral phases including K-bearing minerals, mafic minerals, Fe-oxides, and Fe-hydroxide/oxyhydroxides. Potassium-bearing minerals include alkali feldspar (anorthoclase and sanidine) and a K-bearing phyllosilicate such as illite. The potassium enrichment was likely not from diagenesis but represents variable proportions of sediment from a rock source rich in potassium. Physical sorting may have also played a role in the enrichment in K of the Kimberley formation. The potassic sedimentary rocks examined by the Curiosity rover provide yet additional records of the diversity of the past Martian magmatic activity.

Acknowledgments

This work is supported by the Centre National d'Études Spatiales (CNES), France, and by the NASA Mars Program Office. We gratefully thank the *Curiosity* rover operation team at Jet Propulsion Laboratory for the success of this mission. We also thank Jeff Taylor, our anonymous reviewer, and associate editor for their very thoughtful and thorough comments that greatly improved the manuscript. Imaging and chemical data presented here are available in the NASA Planetary Data System (PDS) http://pds-geosciences.wustl.edu/missions/msl.

References

Ali, A. D., and P. Turner (1982), Authigenic K-feldspar in the Bromsgrove sandstone formation (Triassic) of central England, *J. Sediment. Petrol.*, *52*(1), 187–197.

Anderson, R. B., et al. (2014), Expanded compositional database for ChemCam quantitative calibration, Eighth International Conference on Mars at Caltech, Lunar Planet. Institute, Houston, Tex.

Anderson, R., et al. (2015a), ChemCam results from the Shaler outcrop in Gale Crater, Mars, *Icarus*, *249*, 2–21, doi:10.1016/j.icarus.2014.07.025.

Anderson, R. B., S. M. Clegg, J. Frydenvang, R. C. Wiens (2015b), Sub-model partial least squares for improved accuracy in quantitative laser induced breakdown spectroscopy, Fall AGU, San Francisco, 14-18., Dec.

Bjorkum, P. A., and N. Gjelsvik (1988), An isochemical model for formation of authigenic kaolinite, K-feldspar and illite in sediments, *J. Sediment. Petrol.*, *58*(3), 506–511.

Blaney, D. L., et al. (2014), Chemistry and texture of the rocks at Rocknest, Gale Crater: Evidence for sedimentary origin and diagenetic alteration, *J. Geophys. Res. Planets*, *119*, 2109–2131, doi:10.1002/2013JE004590.

Boynton, W. V., et al. (2007), Concentration of H, Si, Cl, K, Fe, and Th in the low- and mid-latitude regions of Mars, *J. Geophys. Res.*, *112*, E12S99, doi:10.1029/2007JE002887.

Bridges, J. C., S. P. Schwenzer, R. Leveille, F. Westall, R. C. Wiens, N. Mangold, T. Bristow, P. Edwards, and G. Berger (2015), Diagenesis and clay mineral formation at Gale Crater, Mars, *J. Geophys. Res. Planets*, *120*, 1–19, doi:10.1002/2014JE004757.

Bristow, T. F., et al. (2015), The origin and implications of clay minerals from Yellowknife Bay,Gale Crater, Mars, *Am. Mineral.*, *100*, 824–836, doi:10.2138/am-2015-5077.

Carter, J., and F. Poulet (2013), Ancient plutonic processes on Mars inferred from the detection of possible anorthositic terrains, *Nat. Geosci.*, *6*, 1008–1012, doi:10.1038/ngeo1995.

Dehouck, E., and S. M. McLennan (2015), Evaluating the homogeneity oft he X-Ray Amorphous component along the Curiosity rover traverse, European Planet. Sci. Congress 2015, held 27 September-2 October, 2015 in Nantes, Fr. [Available at http://meetingorganizer.copernicus.org/EPSC2015, id. EPSC2015-327.]

Ding, N., V. J. Bray, A. S. McEwen, S. S. Mattson, C. H. Okubo, M. Chojnacki, and L. L. Tornabene (2015), The central uplift of Ritchey crater, Mars, *Icarus*, *252*, 255–270, doi:10.1016/j.icarus.2014.11.001.

Dreibus, G., and H. Wänke (1985), Mars, a volatile-rich planet, *Meteoritics*, *20*, 367–381.

Dreibus, G., and H. Wänke (1987), Volatiles on Earth and Mars—A comparison, *Icarus*, *71*, 225–240.

Fabre, C., et al. (2014), In situ calibration using univariate analyses based on the onboard ChemCam targets: First prediction of Martian rock and soil compositions, *Spectrochim. Acta, Part B*, *99*, 34–51.

Fedo, C. M., I. O. McGlynn, and H. Y. McSween Jr. (2015), Grain size and hydrodynamic sorting controls on the composition of basaltic sediments: Implications for interpreting Martian soils, *Earth Planet. Sci. Lett.*, *423*, 67–77, doi:10.1016/j.epsl.2015.03.052.

Forni, O., S. Maurice, O. Gasnault, R. C. Wiens, A. Cousin, S. M. Clegg, J.-B. Sirven, and J. Lasue (2013), Independent component analysis classification of laser induced breakdown spectroscopy spectra, *Spectrochim. Acta, Part B*, *86*, 31–41, doi:10.1016/j.sab.2013.05.003.

Forni, O., et al. (2015a), First detection of fluorine on Mars: Implications for Gale Crater's geochemistry, *Geophys. Res. Lett.*, *42*, 1020–1028, doi:10.1002/2014GL062742.

Forni, O., et al. (2015b), Fluorine and lithium at the Kimberley outcrop, Gale Crater, Lunar Planet. Sci. XLVI, 1989.

Gasnault, G., J. Taylor, S. Karunatillake, J. Dohm, H. Newsom, O. Forni, P. Pinet, and W. V. Boynton (2010), Quantitative geochemical mapping of Martian elemental provinces, *Icarus*, *207*, 226–247, doi:10.1016/j.icarus.2009.11.010.

Goodrich, C. A., A. H. Treiman, J. Filiberto, J. Gross, and M. Jercinovic (2013), K2O-rich trapped melt in olivine in the Nakhla meteorite: Implications for petrogenesis of nakhlites and evolution of the Martian mantle, *Meteorit. Planet. Sci.*, *48*, 2371–2405.
Grotzinger, J. P., et al. (2014), A habitable fluvio-lacustrine environment at Yellowknife Bay, Gale Crater, Mars, *Science*, *434*(6169), 1242777, doi:10.1126/science.1242777.
Grotzinger, J. P., et al. (2015), Deposition, exhumation, and paleoclimate of an ancient lake deposit, Gale Crater, Mars, *Science*, *350*, doi:10.1126/science.aac7575.
Gupta, S., et al. (2014), Making sense of Martian sediments at the Kimberley, Gale Crater, AGU Fall Meeting, P42C-02.
Hahn, B. C., and S. M. McLennan (2007), Evolution and geochemistry of the Martian crust: Integrating mission datasets, 7th International Conference on Mars, 3179.
Hewins, R. H., and NWA 7533 Consortium (2014), Ancient meteorite breccias on Mars, 77th Annual Meteoritical Society Meeting, 5338.
Humayun, M., et al. (2013), Origin and age of the earliest Martian crust from meteorite NWA753, *Nature*, *503*, 513–516, doi:10.1038/nature12764.
Kiminami, K., and K. Fujii (2007), The relationship between major element concentration and grain size within sandstones from four turbidite sequences in Japan, *Sediment. Geol.*, *195*, 203–215.
Lanza, N. L., et al. (2014), High manganese concentrations in rocks at Gale Crater, Mars, *Geophys. Res. Lett.*, *41*, 5755–5763, doi:10.1002/2014GL060329.
Lanza, N. L., et al. (2015), Oxidation of manganese at Kimberley, Gale Crater: More free oxygen in Mars' past?, Lunar Planet. Sci. XLVI, 2893.
Lasue, J., et al. (2014), ChemCam analysis of Martian fine dust, Lunar Planet. Sci. XLV, 1224.
Lasue, J., et al. (2016), Observation of $>$ 5 wt % Zinc by ChemCam LIBS at the Kimberley, Gale Crater, Mars, *J. Geophys. Res. Planets*, *121*, 338–352, doi:10.1002/2015JE004946.
Le Deit, L., et al. (2015), The potassic sedimentary rocks in Gale Crater, Mars as seen by ChemCam onboard *Curiosity*, Lunar Planet. Sci. Conf. XLVI, Abstract 1438.
Le Mouélic, S., et al. (2015), The ChemCam Remote Micro-Imager at Gale Crater: Review of the first year of operations on Mars, *Icarus*, *249*, 93–107, doi:10.1016/j.icarus.2014.05.030.
Mangold, N., D. Baratoux, O. Arnalds, J.-M. Bardintzeff, B. Platevoet, M. Grégoire, and P. Pinet (2011), Segregation of olivine grains in volcanic sands in Iceland and implications or Mars, *Earth Planet. Sci. Lett.*, *310*, 233–243, doi:10.1016/j.epsl.2011.07.025.
Mangold, N., et al. (2015), Chemical variations in Yellowknife Bay formation sedimentary rocks analyzed by ChemCam on board the *Curiosity* rover on Mars, *J. Geophys. Res. Planets*, *120*, 452–482, doi:10.1002/2014JE004681.
Mangold, N., et al. (2016), Composition of conglomerates analyzed by the Curiosity rover: Implications for Gale Crater crust and sediment sources, *J. Geophys. Res. Planets*, *121*, doi:10.1002/2015JE004977.
Maurice, S., et al. (2012), The ChemCam instrument suite on the Mars Science Laboratory (MSL) rover: Science objectives and mast unit description, *Space Sci. Rev.*, *170*, 95–166, doi:10.1007/s11214-012-9912-2.
McLennan, S. M., et al. (2013), Elemental geochemistry of sedimentary rocks in Yellowknife Bay, Gale Crater, Mars, *Science*, *343*(6169), 1244734, doi:10.1126/science.1244734.
Meslin, P.-Y., et al. (2013), Soil diversity and hydration as observed by ChemCam at Gale Crater, Mars, *Science*, *341*(6153), 1238670, doi:10.1126/science.1238670.
Nekvasil, H., J. Filiberto, F. M. McCubbin, and D. H. Lindsley (2007), Alkalic parental magmas for the chassignites?, *Meteorit. Planet. Sci.*, *42*, 979–992.
Ollila, A. M., et al. (2014), Trace element geochemistry (Li, Ba, Sr, and Rb) using *Curiosity*'s ChemCam: Early results for Gale Crater from Bradbury Landing Site to Rocknest, *J. Geophys. Res. Planets*, *119*, 255–285, doi:10.1002/2013JE004517.
Palucis, M. C., W. E. Dietrich, A. G. Hayes, R. M. Williams, S. Gupta, N. Mangold, H. Newsom, C. Hardgrove, F. Calef III, and D. Y. Sumner (2014), The origin and evolution of the Peace Vallis fan system that drains to the *Curiosity* landing area, Gale Crater, Mars, *J. Geophys. Res. Planets*, *119*, 705–728, doi:10.1002/2013JE004583.
Sautter, V., et al. (2013), Is Bathurst Inlet rock an evidence of explosive volcanism in the Rocknest area of Gale Crater?, Lunar Planet. Sci. XLIV, 1985.
Sautter, V., et al. (2015), In situ evidence for continental crust on early Mars, 8(8):605–609, *Nat. Geosci.*, doi:10.1038/ngeo2474.
Sautter, V., et al. (2016), Magmatic complexity on early Mars as seen through a combination of orbital, in-situ and meteorite data, *Lithos*, *254-255*, 36–52.
Schmidt, M. E., et al. (2014), Geochemical diversity in first rocks examined by the *Curiosity* rover in Gale Crater: Evidence for and significance of an alkali and volatile-rich igneous source, *J. Geophys. Res. Planets*, *119*, 64–81, doi:10.1002/2013JE004481.
Schmidt, M. E., N. Mangold, M. Fisk, O. Forni, S. McLennan, D. W. Ming, D. Sumner, V. Sautter, A. J. Williams, and R. Gellert (2015), Classification scheme for diverse sedimentary and igneous rocks encountered by MSL in Gale Crater, Lunar Planet. Sci. XLVI, 1566.
Schröder, S., et al. (2015), Hydrogen detection with ChemCam at Gale Crater, *Icarus*, *249*, 43–61, doi:10.1016/j.icarus.2014.08.029.
Siebach, K., J. P. Grotzinger, S. M. Mclennan, M. B. Baker, R. Gellert, J. A. Hurowitz, and D. L. Blaney (2015), Sorting out APXS compositional variations in Gale Crater sedimentary rocks, Mars, GSA annual meeting, Baltimore, Abstract 94-2.
Stack, K. M., et al. (2016), Comparing orbiter and rover image-based mapping of an ancient sedimentary environment, Aeolis Palus, Gale Crater, Mars, *Icarus*, doi:10.1016/j.icarus.2016.02.024.
Stolper, E. M., et al. (2013), The petrochemistry of Jake_M: A Martian mugearite, *Science*, *341*, doi:10.1126/science.1239463.
Taylor, G. J., et al. (2006), Bulk composition and early differentiation of Mars, *J. Geophys. Res.*, *111*, E03S10, doi:10.1029/2005JE002645.
Taylor, S. R., and S. M. McLennan (2009), *Planetary Crusts: Their Composition, Origin and Evolution*, Cambridge Univ. Press, Cambridge, U. K.
Treiman, A. H., et al. (2016), Mineralogy, provenance, and diagenesis of a potassic basaltic sandstone on Mars: CheMin X-ray diffraction of the Windjana Sample (Kimberley Area, Gale Crater), *J. Geophys. Res. Planets*, *121*, 75–106, doi:10.1002/2015JE004932.
Vaniman, D. T., et al. (2014), Mineralogy of a mudstone at Yellowknife Bay, Gale Crater, Mars, *Science*, (6169), 1243480, 343, doi:10.1126/science.1243480.
Wiens, R. C., et al. (2012), The ChemCam instrument suite on the Mars Science Laboratory (MSL) rover: Body unit and combined system tests, *Space Sci. Rev.*, *170*, 167–227, doi:10.1007/s11214-012-9902-4.
Wiens, R. C., et al. (2013), Pre-flight calibration and initial data processing for the ChemCam laser-induced breakdown spectroscopy instrument on the Mars Science Laboratory rover, *Spectrochim. Acta, Part B*, *82*, 1–27, doi:10.1016/j.sab.2013.02.003.
Williams, R. M. E., et al. (2013), Martian fluvial conglomerates at Gale Crater, *Science*, *340*, 1068–1072.
Wittmann, A., R. L. Korotev, B. L. Jolliff, A. J. Irving, D. E. Moser, I. Barker, and D. Rumble III (2015), Petrography and composition of Martian regolith breccia meteorite North-west Africa 7475, *Meteorit. Planet. Sci.*, *50*, 326–352, doi:10.1111/maps.12425.
Wray, J. J., S. T. Hansen, J. Dufek, G. A. Swayze, S. L. Murchie, F. P. Seelos, J. R. Skok, R. P. Irwin III, and M. S. Ghiorso (2013), Prolonged magmatic activity on Mars inferred from the detection of felsic rocks, *Nat. Geosci.*, *6*, 1013–1017, doi:10.1038/ngeo1994.